

Bachelor thesis



Czech
Technical
University
in Prague

F4

Faculty of Nuclear Sciences and Physical Engineering
Department of Physics

Detachment tomographic inversion study with fast visible cameras on the COMPASS tokamak

Michal Odložilík

Supervisor: Dr. Jordan Cavalier

Consultant: Ing. Jakub Svoboda

Study programme: Physical engineering

Specialization: Plasma Physics and Thermonuclear Fusion

August 2023



BACHELOR THESIS ASSIGNMENT

Academic year: 2022/2023

Student: Michal Odložilík

Study programme: Physical Engineering

Specialization: Physics of Plasma and Thermonuclear Fusion

Thesis title:
(in Czech) Tomografická inverze viditelného záření detekovaného kamerami s vysokou snímkovací frekvencí pro studium detachmentu v tokamaku COMPASS

Thesis title:
(in English) Detachment tomographic inversion study with fast visible cameras on the COMPASS tokamak

Language of the Thesis: English language

Instructions:

- 1) Learn how to model the camera view thanks to the Calcam software.
- 2) Perform tomographic inversion of camera data with existing Python programs.
- 3) Analyse different plasma scenarios.
- 4) Possibly improve the tomography inversion by for e.g using different tomography algorithm and accounting reflections.

Recommended literature:

- [1] J. Cavalier et al.: Tomographic reconstruction of tokamak edge turbulence from single visible camera data and automatic turbulence structure tracking, Nucl. Fusion 59, 2019, 056025
- [2] J. Svoboda et al.: Tomotok: python package for tomography of tokamak plasma radiation, JINST 16, 2021, C12015
- [3] L. C. Ingesson, B. Alper, B. J. Peterson & J.-C. Vallet: Chapter 7: Tomography Diagnostics: Bolometry and Soft-X-Ray Detection, Fusion Science and Technology, 2008, 53:2, 528-576
- [4] M Anton et al.: X-ray tomography on the TCV tokamak, Plasma Phys. Control. Fusion 38, 1996, 1849

Name and affiliation of the supervisor:

Dr. Jordan Cavalier,
Institute of Plasma Physics of the CAS


Name and affiliation of the consultant:

Ing. Jakub Svoboda, Department of Physics, Faculty of Nuclear Sciences and Physical Engineering of the CTU in Prague

Date of the assignment: 20.10.2022

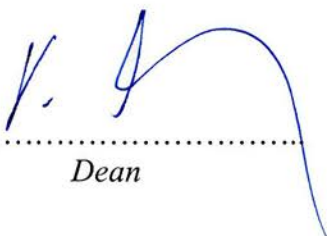
Due date of the thesis: 02.08.2023

The assignment is valid for two years since the date of the assignment


.....
Guarantor of the study programme




.....
Department head


.....
Dean

In Prague on 20.10.2022

ZADÁNÍ BAKALÁŘSKÉ PRÁCE

Akademický rok: 2022/2023



Student: Michal Odložilík

Studijní program: Fyzikální inženýrství

Specializace: Fyzika plazmatu a termojaderné fúze

Název práce: Tomografická inverze viditelného záření detekovaného kamerami s vysokou snímkovací frekvencí pro studium detachmentu v tokamaku COMPASS
(česky)

Název práce: Detachment tomographic inversion study with fast visible cameras on the COMPASS tokamak
(anglicky)

Jazyk práce: Angličtina

Pokyny pro vypracování:

- 1) Naučit se modelovat obraz z kamery díky softwaru Calcam.
- 2) Provést tomografickou inverzi dat z kamery pomocí dostupných programů v jazyce Python.
- 3) Analyzovat různé scénáře průběhu plazmatu.
- 4) Případně vylepšit tomografickou inverzi např. použitím jiného tomografického algoritmu a zohledněním odrazů.

Doporučená literatura:

- [1] J. Cavalier et al.: Tomographic reconstruction of tokamak edge turbulence from single visible camera data and automatic turbulence structure tracking, Nucl. Fusion 59, 2019, 056025
- [2] J. Svoboda et al.: Tomotok: python package for tomography of tokamak plasma radiation, JINST 16, 2021, C12015
- [3] L. C. Ingesson, B. Alper, B. J. Peterson & J.-C. Vallet: Chapter 7: Tomography Diagnostics: Bolometry and Soft-X-Ray Detection, Fusion Science and Technology, 2008, 53:2, 528-576
- [4] M Anton et al.: X-ray tomography on the TCV tokamak, Plasma Phys. Control. Fusion 38, 1996, 1849

Jméno a pracoviště vedoucího bakalářské práce:

Dr. Jordan Cavalier, Ústav fyziky plazmatu AV ČR, v. v. i.

Jméno a pracoviště konzultanta:

Ing. Jakub Svoboda

Katedra fyziky, Fakulta jaderná a fyzikálně inženýrská ČVUT v Praze

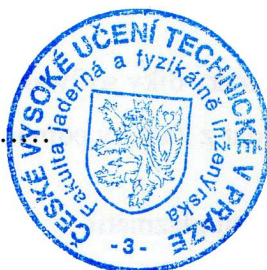
Datum zadání bakalářské práce: 20.10.2022

Termín odevzdání bakalářské práce: 02.08.2023

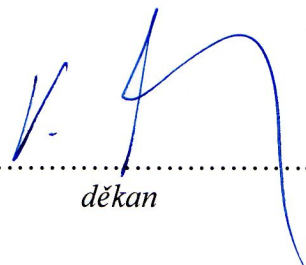
Doba platnosti zadání je dva roky od data zadání.



.....
garant studijního programu



.....
vedoucí katedry



.....
děkan

V Praze dne 20.10.2022



PROHLÁŠENÍ

Já, níže podepsaný

Jméno a příjmení studenta: Michal Odložilík
Osobní číslo: 502401
Název studijního programu (oboru): Fyzikální inženýrství

prohlašuji, že jsem bakalářskou práci s názvem:

Tomografická inverze viditelného záření detekovaného kamerami s vysokou snímkovací frekvencí pro studium detachmentu v tokamaku COMPASS

vypracoval(a) samostatně a uvedl(a) veškeré použité informační zdroje v souladu s Metodickým pokynem o dodržování etických principů při přípravě vysokoškolských závěrečných prací.

V Praze dne 29.7.2023

podpis

Acknowledgements

I would like to express my gratitude to my supervisor Dr. Jordan Cavailer, for his guidance of my bachelor thesis, valuable comments and remarks that helped me to improve the quality of my work. I would also like to thank Ing. Jakub Svoboda for consultations, help with data processing and support.

Declaration

I declare that I have prepared my bachelor thesis independently and have used only the materials (literature, projects, software, etc.) listed in the attached list.

Prague, August 2, 2023

Prohlašuji, že jsem svou bakalářskou práci vypracoval samostatně a použil jsem pouze podklady (literaturu, projekty, SW atd.) uvedené v příloženém seznamu.

V Praze, 2. srpna 2023

Abstract

The most stressed part of tokamak, in terms of particle and heat flux, is the divertor. To ease this stress, the detachment is implemented by seeding suitable gas impurities to the divertor area. These impurities then dissipate energy of the fluxes by radiation, which could be measured with fast visible cameras and subsequently analysed. This thesis deals with the processing of the camera signal from the detachment experiments on the COMPASS tokamak, by applying tomographic inversion of single camera data on different plasma scenarios, and studies the application of various tomographic inversion algorithms.

Keywords: tomographic inversion, fast visible cameras, tokamak, detachment, plasma

Supervisor: Dr. Jordan Cavalier
Ústav fyziky plazmatu Akademie věd
České republiky,
U Slovanky 2525/1a,
Praha 8

Consultant: Ing. Jakub Svoboda

Abstrakt

Nejvíce zatíženou částí tokamaku z hlediska toku částic a tepla je divertor. Aby se toto zatížení zmírnilo, zavádí se tzv. detachment, přidáním vhodných plynných příměsí do oblasti divertoru. Tyto nečistoty pak disipují energii toků pomocí záření, které lze měřit kamerami s vysokou snímkovací frekvencí a následně analyzovat. Tato práce se zabývá zpracováním kamerového signálu z experimentů detachmentu na tokamaku COMPASS pomocí tomografické inverze dat jedné kamery, při různých průbězích plazmatu, a studuje použití odlišných algoritmů tomografické inverze.

Klíčová slova: tomografická inverze, kamery s vysokou snímkovací frekvencí operující ve viditelném spektru, tokamak, detachment, plazma

Překlad názvu: Tomografická inverze viditelného záření detekovaného kamerami s vysokou snímkovací frekvencí pro studium detachmentu v tokamaku COMPASS

Contents

1 Introduction	1
1.1 Tokamak principle	2
1.2 Divertor detachment	4
1.3 Tomography principle	5
2 Detachment experiments at the COMPASS tokamak	9
2.1 The COMPASS tokamak	9
2.2 RIS camera diagnostics on the COMPASS tokamak	10
2.3 Divertor detachment at the COMPASS tokamak	14
2.4 Forward and reversed field detachment discharges	16
3 Procedure for camera tomography of tokamak plasmas	21
3.1 Camera view calibration	22
3.2 Tomography of single camera observation	23
3.3 Discretization and geometry matrix	24
3.4 Inversion algorithms	27
3.4.1 Minimum Fisher Regularization	28
3.4.2 Biorthogonal basis decomposition	29
4 Issues and solutions for tomographic inversion of camera data	33
4.1 Preliminary analysis	33
4.2 Camera view selection	35
4.3 Pixel selection and mesh grid adjustment	36
4.4 Error estimation for Minimum Fisher Regularization	38
5 Tomography applied to the detachment experiments	39
5.1 Forward fields discharge #15977	39
5.2 Reversed fields discharge #20919	40
5.3 Toroidal symmetry investigation	45
5.4 Discussion on the accuracy of the reconstructions	48
Summary and conclusion	51
Bibliography	53
A Additional figures	57

Chapter 1

Introduction

Energy production has always been one of the vital sectors of development and industry. There are different ways to generate energy, such as burning fossil fuels, splitting atoms or using renewable sources. Nevertheless, each of these methods possesses significant drawbacks. Fossil fuels are cheap and abundant, but they pollute the environment and will eventually run out. Nuclear fission is an alternative, but its fuel is expensive and scarce, and it creates radioactive waste in the process. Renewable sources are clean and affordable, but they are not enough to meet the demand at all times and they depend on variable factors like weather or geography. Therefore it would be desirable to find a new type of energy, that could fulfil the demand all the times, without generating any pollution and its fuel would be abundantly available. Fusion energy could be a potential solution to these requirements.

Fusion energy is gained from the nuclear fusion, which is a process of merging lighter nuclei into heavier, that could be followed by an energy release. If this process could be effectively controlled and sustained, it would offer a potential source of energy in fusion reactors. To acquire nuclear fusion, usually tritium ^3H and deuterium ^2H is used as a fuel. These isotopes are used because they have favourable cross sections of their fusion reactions in conditions, that are achievable in fusion devices. To reach these conditions, fusion fuel must be heated to extreme temperatures that turns it into plasma. There are two main ways to make and confine this plasma, each based on a different approach of fulfilling the necessary conditions. First is the inertial confinement, which uses powerful lasers to create high density and temperatures of the fuel in a short time, allowing the nuclei to fuse and release energy. The second approach is the magnetic confinement, which uses strong magnetic fields to keep the energy and plasma in one place, allowing the fuel to continuously burn through fusion, gaining an energy in process. Currently, the magnetic confinement has more explicit plans for possible commercial use. One of the roadmaps can be seen in Fig. 1.1

The two main types of devices that are using the magnetic confinement and have best results are the stellarators and tokamaks. Both work on similar principles, but have different configuration of magnetic field. Stellarators use very complex magnetic field geometries to confine the plasma, requiring coils that are difficult to design. This may make stellarators more efficient than

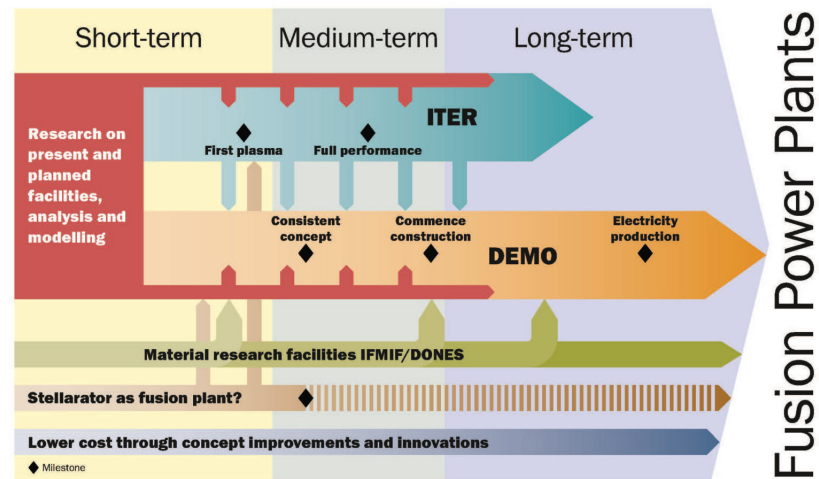


Figure 1.1: The EUROfusion roadmap plan for commercial energy from fusion. Image taken from [1].

tokamaks, but today they are not as widespread because of this.

One of the problems all fusion devices encounter is high heat and particle fluxes caused by the extreme conditions and nuclear reactions. This causes serious risk of damage to the material. Tokamak usually solves this problem by introducing the divertor configuration and other mechanisms to counter the fluxes.

A variety of diagnostics are then used on tokamaks for tasks ranging from feedback control to basic physical studies, one of which is the tomography. This diagnostic allows to study different profiles of plasma and radiation structures, without affecting the processes itself. However, tomography is also quite complicated, requiring several conditions to be met and the use of some special methods to produce results.

The aim of this thesis is to present the results of the detachment tomography study on the COMPASS tokamak, provide theoretical background and describe the used procedures.

In next sections, basic description of tokamak, divertor detachment and tomography is presented, to give general overview to the topic of this thesis.

1.1 Tokamak principle

The tokamak is a device that is using strong magnetic fields to confine the plasma. Basic scheme of tokamak is shown in Fig. 1.2.

Tokamak's toroid configuration allows the creation of helical magnetic field. To create this field, combination of different coils and central solenoid is used. The main part of the tokamak is the vacuum chamber, in which the gas is located (usually isotope of hydrogen) from which the plasma is created. The chamber is surrounded by toroidal field coils, that are capable of producing strong toroidal field. Then by using central solenoid as a primary circuit

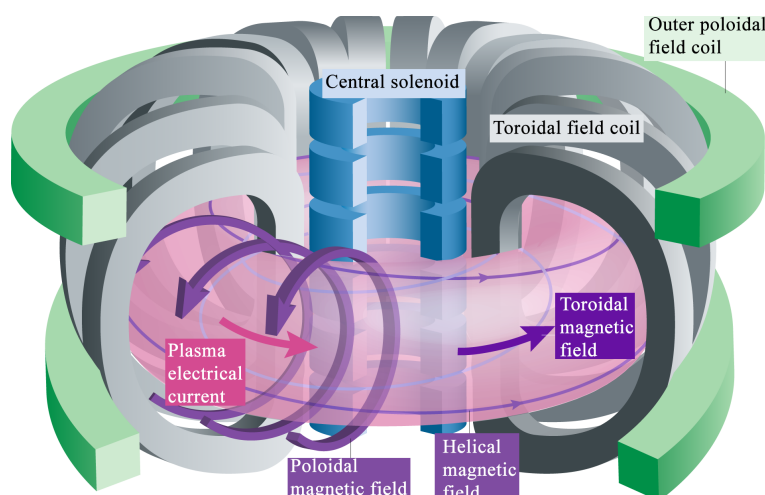


Figure 1.2: Basic scheme of tokamak. Central solenoid generates plasma current in plasma (pink), creates the poloidal magnetic field by induction. The toroidal field coils generate the toroidal field and poloidal coils further stabilise the plasma and shape the magnetic field. The result of toroidal and poloidal magnetic field is helical field. Edited image taken from [2].

and the plasma as a secondary circuit, the plasma current could be created, which also produces poloidal magnetic field. Combining the poloidal and toroidal magnetic fields, helical magnetic field is formed. However this simple configuration is not stable - instabilities occur. Various combinations of outer poloidal field coils are used to counter instabilities and shape the plasma. Additional coils are then used to further shape the confined plasma into the desired shape.

Tokamaks, as other fusion devices, create large amount of heat and particle fluxes during its operation. These fluxes could easily damage any ordinary material. To direct the energy and particle to an area which is specifically designed to withstand these fluxes, divertor configuration is implemented. This configuration allows magnetic field to be shaped as shown in Fig. 1.3. In this configuration, the border of the confined area with closed magnetic field lines is known as separatrix (also called Last Closed Flux Surface (LCFS)). On the other hand, the outer region, between the chamber wall and separatrix, is called the Scrape-Off Layer (SOL). In the SOL, magnetic field lines are open, touching the first wall and plasma that enters it could be scraped off. SOL also absorbs most of the particle and heat exhaust from plasma, which is then diverted towards the divertor plates [3].

Divertor target area is therefore the most stressed part of the tokamak in terms of heat and particle fluxes, which could cause serious material damage to the Plasma Facing Components (PFCs). To prevent this damage, many solutions are being implemented.

Currently, the most widely researched solutions that address these problems are:

- Liquid metal divertor, where flowing liquid metals are used as PFCs,

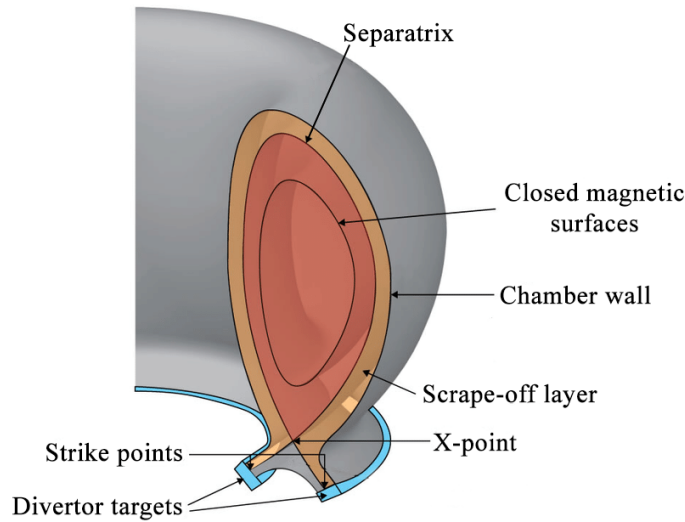


Figure 1.3: Scheme of typical magnetic field in divertor configuration, where the two connection points of the separatrix and the divertor are called strike points. Edited image courtesy of EUROfusion.

renewing the plasma facing material before it gets eroded [4].

- Strike point sweeping, which spreads the heat load to a larger area [5].
- Divertor detachment, which uses detached plasma to mitigate the plasma power and ion flux, before it reaches the target.

There still exist other methods, but this thesis focuses on divertor detachment, which is introduced in the next chapter.

1.2 Divertor detachment

The divertor detachment is based on the idea to dissipate the energy away from the divertor plates, to screen off the divertor from incoming fluxes by puffing some gas.

In general, there are two ways to achieve this detached regime. The first one is to increase the density until a sufficient number of collisions with charged and neutral particles occur, that lead to a power dissipation and cooling of the plasma that could interact with the PFCs. The second method, on which this thesis will be focusing, is based on injections of selected impurities, often strong radiators, that allow the particle fluxes to radiate significant part of its energy before they reach the PFCs.

The impurities cause strong reduction of plasma ions flux onto the target and the plasma pressure drop along magnetic field lines towards the divertor target. During detachment, near the divertor target, several regions based on particle interactions can be distinguished, as shown in Fig. 1.4. In the radiation region, charged particles interact through collisions with the impurities and lose majority of their energy by radiation. The ionisation region is the part

where the injected gas is getting ionised by the incoming particle flux. After passing the ionisation region, charged particles enter the recombination region, the ions recombine with electrons thanks to the lower temperatures [6]. This causes the density and pressure near the target to be considerably lower than they would be without the detachment and the power to be radiated over the whole first wall area, instead of only locally to the divertor target.

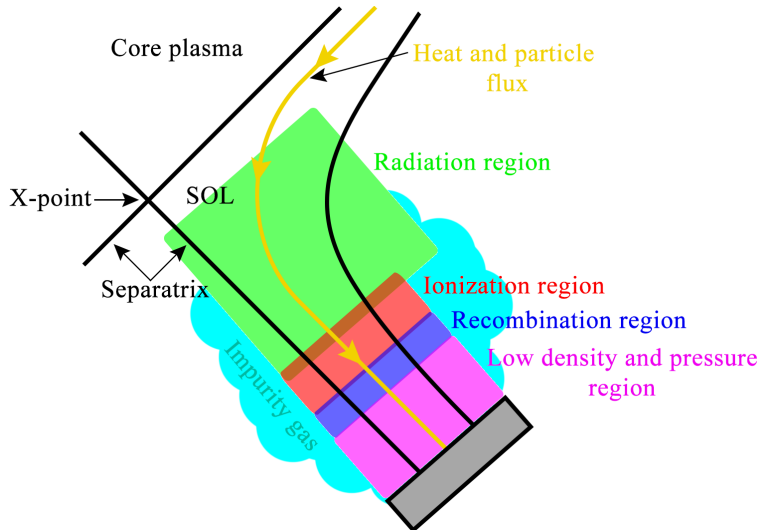


Figure 1.4: Scheme of regions close to the target during the divertor detachment. Size and locations of regions are approximate and only for illustration.

On the ITER tokamak, and other tokamaks planned for future, detached or partially detached regime is planned to be implemented [7]. Therefore experiments involving the detachment are vital part for future commercial use of fusion energy. Overall, the physics of the detachment is very complex, which is why this matter is intensively studied by a wide range of diagnostics.

1.3 Tomography principle

The tomography is a type of cross-sectional imaging. The name itself comes from two Greek words "tomos" and "graphos", translated "slice" and "drawing" [8]. It uses several projections of an observed object to reconstruct its cross section as is illustrated in Fig. 1.5. The observed objects are in this case geometric shapes inside the box and their projections P are usually the measured data. However, in order to obtain the cross sections S_1 and S_2 by tomographic inversion, an infinite number of observed P projections is needed.

In practice it is then necessary to measure as many projections as possible, or constrain their number by making some strong assumptions. A typical example of the inversion problem is Radon transform [10]. Basic scheme of this method is shown in Fig. 1.6. This method consists in varying the position and angles of the radiation source in order to obtain different projections,

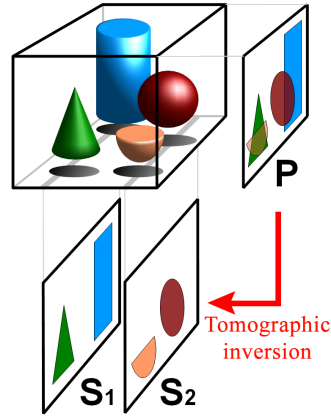


Figure 1.5: Tomographic inversion principle illustration. P is a projection of the observed objects, S_1 and S_2 are then the slices retrieved by tomographic inversion from the projection P . Edited image taken from [9].

from which images of the slices can be retrieved by inversion.

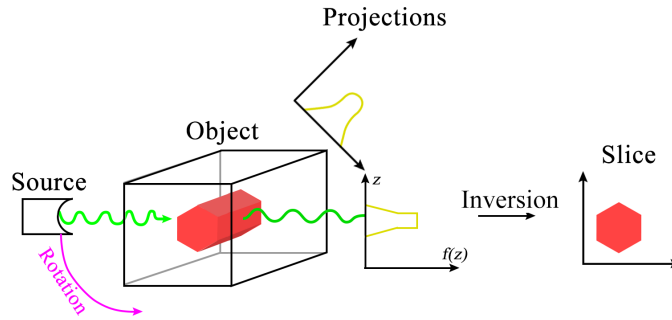


Figure 1.6: Example of reconstruction via the Radon transform using observations from different angles. The applied inversion to the projection data then reconstructs the slice image. Image recreated from [10].

In tokamaks, the method of radon transform is not typically used for tomography. Instead, other methods are implemented to reconstruct the plasma's emissivity profile using the electromagnetic radiation naturally emitted by the plasma. The radiation could be recorded by metallic foil bolometers, photodiode arrays or even fast visible cameras. In general the measured signal by one element of the detector could be written as [11]:

$$f_i = \int T_i(\mathbf{r}) S_0(\mathbf{r}) d\mathbf{r}, \quad (1.1)$$

where f_i is the measured signal by i^{th} element of the detector, \mathbf{r} is position vector and $T_i(\mathbf{r})$ is a term that describes the geometry. To solve the tomography problem, assumptions of symmetry and other approximations are often used, that eventually allow the tomographic inversion to be performed. The tomography problem after discretization and numerical approach then could be written as [11]:

$$\mathbf{f} = \mathbf{T} \cdot \mathbf{S}_0, \quad (1.2)$$

where \mathbf{f} are values collected by all elements of the detector, \mathbf{T} is the geometry matrix containing the information about the geometry and \mathbf{S}_0 is the discretized emissivity function. The aim of tomographic inversion is then to retrieve the emissivity \mathbf{S}_0 , from the measured function \mathbf{f} consisting of elements f_i . The emissivity profile function \mathbf{S}_0 then holds the information about the density, temperature or other properties of the plasma.

Chapter 2

Detachment experiments at the COMPASS tokamak

This chapter focuses on the detachment experiments that were performed on the COMPASS tokamak. The first section describes the COMPASS tokamak and its main parameters, followed by the description of RIS camera diagnostics (used for the tomography analysis), detachment experiments and the examined discharges.

2.1 The COMPASS tokamak

The COMPASS tokamak was located at Institute of Plasma Physics of the CAS in Prague (IPP) and was decommissioned in 2021 after ten years of operation, to be replaced by a more advanced tokamak called COMPASS Upgrade. Its characteristic parameters are listed in Tab. 2.1 and plasma cross section with comparison to other tokamaks is shown in Fig. 2.1. The COMPASS tokamak belonged to the compact tokamaks, that were capable of high confinement operation (H-mode), with plasma shape corresponding to one tenth of the plasma in ITER. At the time of its operation, only two other tokamaks with ITER-like configurations capable of reaching H-mode were in Europe.

Parameters	Values
Major radius R	0.56 m
Minor radius a	0.23 m
Plasma current I_p (max)	400 kA
Magnetic field B_t (range)	0.9-2.1 T
Vacuum pressure	1×10^{-6} Pa
Elongation	1.8
Plasma shape	D, SND, ellipse, circle
Beam heating P_{NBI} 40 keV	2×0.4 MW, 1×1 MW
Discharge length	~ 1 s

Table 2.1: Main parameters of the COMPASS tokamak. [12]

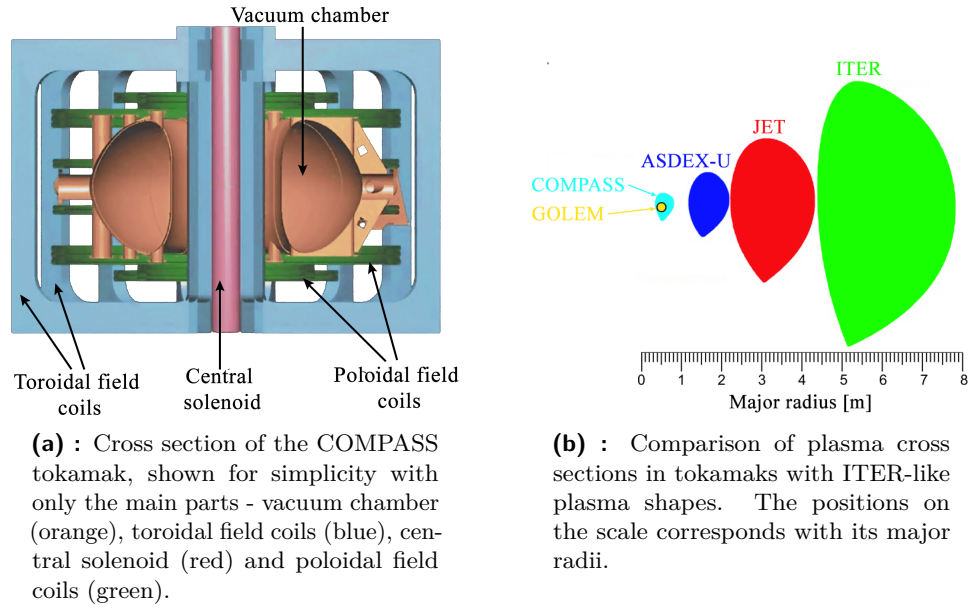


Figure 2.1: Cross section (a) and comparisons (b) of the COMPASS tokamak with other tokamaks. Edited images taken from [12].

Most of the research conducted at the IPP tokamak division are focusing on development of new diagnostics and edge plasma studies, which includes studies of detachment. Therefore, a wide range of diagnostics were installed for research purposes, including magnetic, microwave, spectroscopic, probe or beam and particle diagnostics. All of them allowed in-depth study of the plasma and its processes. This thesis focuses on exploitation of the data captured by Rapid Imaging System (RIS) diagnostics, consisting of two fast colour visible cameras.

2.2 RIS camera diagnostics on the COMPASS tokamak

Rapid Imaging System (RIS) is a fast video camera system consisting of two fast colour visible cameras of the Photron FASTCAM Mini UX100 type [13], providing plasma-neutral and plasma-wall interaction overview, in captured videos.

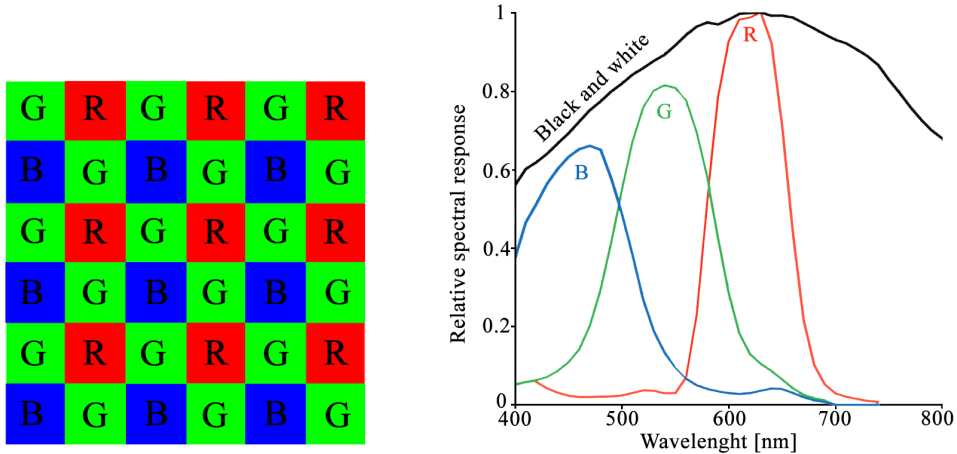
The main parameters of the RIS cameras are shown in Tab. 2.2. These CCD sensor cameras are able to record videos in maximal 1280x1024 pixel resolution, with frame rates up to 800 kfps (kilo frames per second) with reduced resolution. The frame rate performance depends on the resolution, meaning that fast events have to be observed in lower resolution for proper analysis. In the Tab. 2.2 the first four frame rates (up to 6400fps) are the typical values for ordinary overview of the discharge, that were also used in videos analysed in this thesis (with exposure time around 200 microseconds).

The RIS cameras are 12 bits, equipped with Bayer-type sensors [15] working

Fastcam Photron Mini UX100	
Sensor	CCD, 1280 x 1024 pixels, 10um pixel size, Bayer system
Resolution	Frame rate performance
1280x1024px	1000fps
1280x1000px	5000fps
896x800px	4000fps
768x704px	6400fps
640x8	800000fps
Spectral range	~ 300-700nm
Bit depth	12 bit (for every R, G and B component)

Table 2.2: Selected parameters of used RIS cameras [14].

in the visible spectrum ($\sim 300\text{-}700\text{ nm}$). These sensors are made of pixel mosaic, where each pixel detect different spectrum of colours. The mosaic, i.e. Bayer filter, that is used on RIS camera is shown in Fig. 2.2a. The pixels have different sensitivity for each colour. This relation is then showed in Fig. 2.2b.



(a) : GRBG Bayer filter.

(b) : Fastcam Mini UX100 relative spectral response curves for given wavelengths. The black curve corresponds to monochrome colour, the other curves corresponds to red, green and blue colours. Edited graph taken from camera manual [14].

Figure 2.2: The RIS camera Bayer filter and the colour sensitivity.

The optics are then needed to see the plasma and to guide the light through the port to the camera chip. They also determine the extend of the field of view. The RIS1 camera then provides large toroidal view observing both sides of the tokamak and the RIS2 camera provides tangential view. The approximate setup and field of views of the cameras is shown in Fig. 2.3.

During the impurity injection experiments, the RIS1 camera had view on the area of injection, whereas the RIS2 camera is facing the opposite side of the chamber, with, therefore, no view on the injection. It is important for the possible broken symmetry that gas injection perturbation could imply.

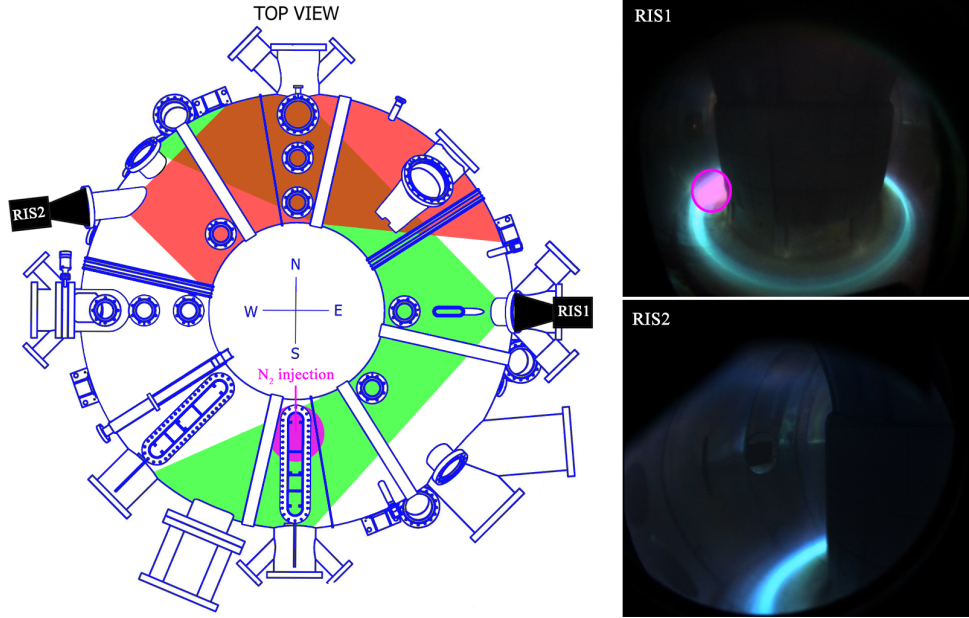


Figure 2.3: Approximate positions and field of views of RIS1 (green) and RIS2 (red) cameras shown from the top view of the vacuum chamber, with corresponding images captured during nitrogen experiment study. The nitrogen gas injection region is highlighted (pink) in the top view of the RIS1 captured image, which RIS2 does not observe.

The process of demosaicing is usually applied on the recorded images, to obtain an image somewhat similar to what the naked eye would observe. This process interpolates the area around each coloured pixel to get RGB values corresponding to eye observation. The resulting image then looks as if seen by the human eye. An image before and after demosaicing of the RIS2 camera can be seen in Fig. 2.4. For the image data processing or tomography, raw data before demosaicing are used.

The Bayer filter allows to decompose the image to four colour components at a cost of resolution reduction to 1/4 of the original resolution, thus allowing to work in a certain colour spectrum. An example of decomposed image can be seen in Fig. 2.5.

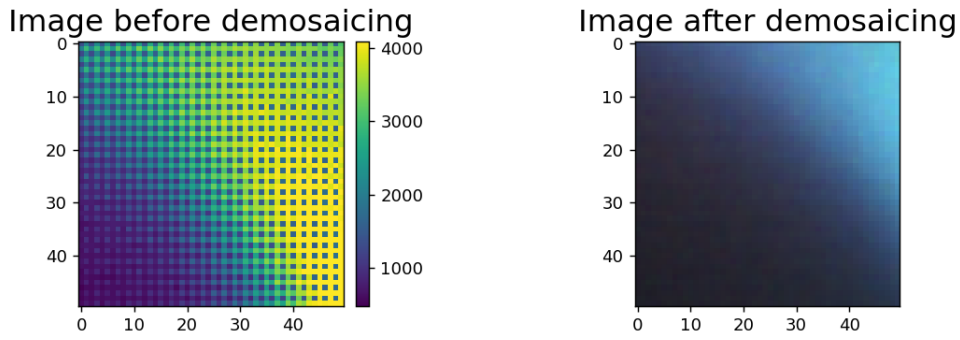


Figure 2.4: Zoom on the raw image before demosaicing (left) and the same zoom after demosaicing (right), captured by RIS2 camera.

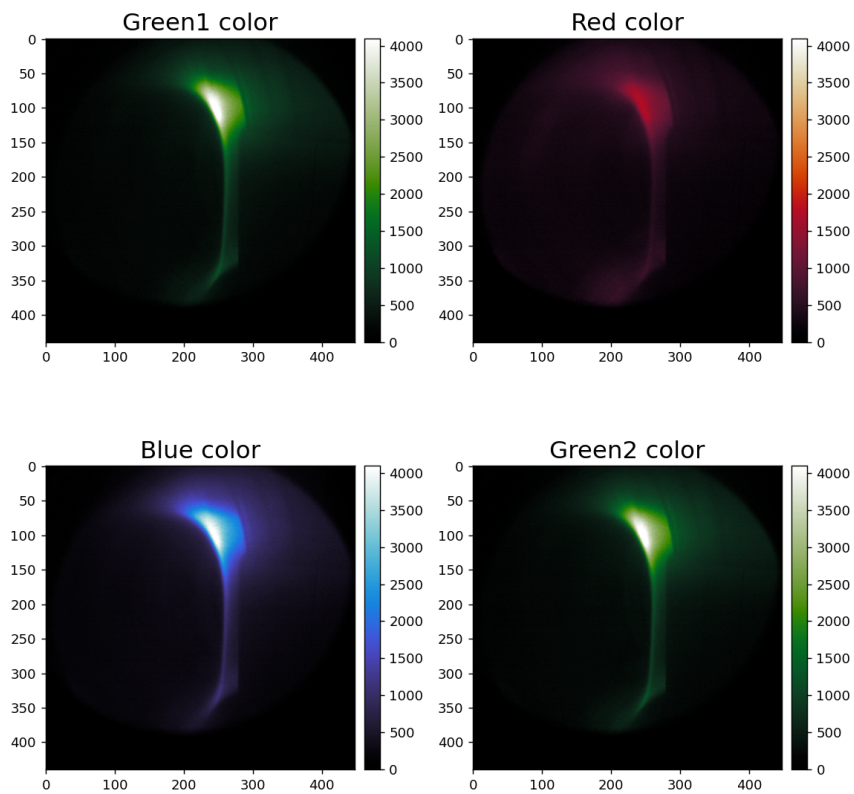


Figure 2.5: Example of colour decomposition on RIS camera image. The image comes from RIS2 camera, discharge #20919, $t=1220.125\text{ms}$.

2.3 Divertor detachment at the COMPASS tokamak

At the COMPASS tokamak, series of experiments on impurity injections were conducted to study the detached regimes [16, 17]. The impurity gases were injected into ohmic or neutral beam injector (NBI)-heated low confinement plasmas, and also H-mode discharges. All discharges presented in the thesis were part of L-mode discharges. A simplified schematic of the experiments is depicted in Fig. 2.6.

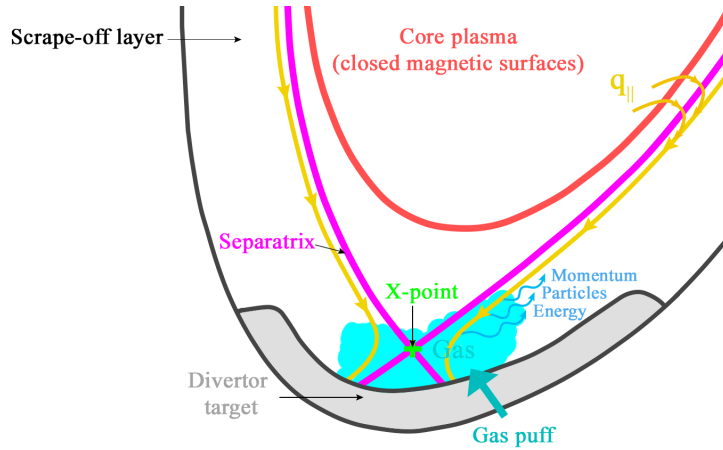


Figure 2.6: Schematic of typical detachment experiment at the COMPASS tokamak. The core plasma is confined inside the separatrix and the parallel flux $q_{||}$ is directed in SOL towards the divertor target. The gas is injected towards the X-point and the incoming plasma particle and energy fluxes interact with the injected gas, followed by partial loss of the momentum, particles and energy.

On COMPASS, the detachment was studied using different impurity gases that were all strong radiators. Nitrogen was used in the first set of experiments and argon and neon in the second set. The goal was to achieve a mitigation of the parallel heat fluxes $q_{||}$ while maintaining the confinement of the core plasma. Appropriate scenarios were achieved, so that there was no radiative collapse of the plasma when an appropriate seeding injection waveform was implemented. From the three studied impurities, nitrogen performed the best [17]. Nitrogen impurity caused the heat flux to the target to be the lowest, with the lowest pressure at the divertor. Nevertheless, the neon and argon also performed relatively well.

The power falling into divertor can be characterised by peak heat flux q_{peak} and the divertor power fraction f_{div} . In Fig. 2.7 these two quantities are shown as a function of the radiated fraction f_{rad} and for different gas injected. The definitions of these parameters can be found in [16], but are recalled here for clarity.

Radiation fraction f_{rad} is defined as:

$$f_{\text{rad}} = \frac{P_{\text{rad}}}{P_{\text{ohm}} + P_{\text{NBI}}} \quad (2.1)$$

where P_{rad} is the total radiated power measured by bolometry, P_{ohm} is the ohmic input power and P_{NBI} the power input from NBI. The peak heat flux q_{peak} is defined as a maximum of heat flux at the outer target and the divertor power fraction f_{div} is the fraction of power crossing the separatrix which finally reaches the divertor target. A reduction of both these quantities means that part of the incoming fluxes is radiated on the way to the divertor.

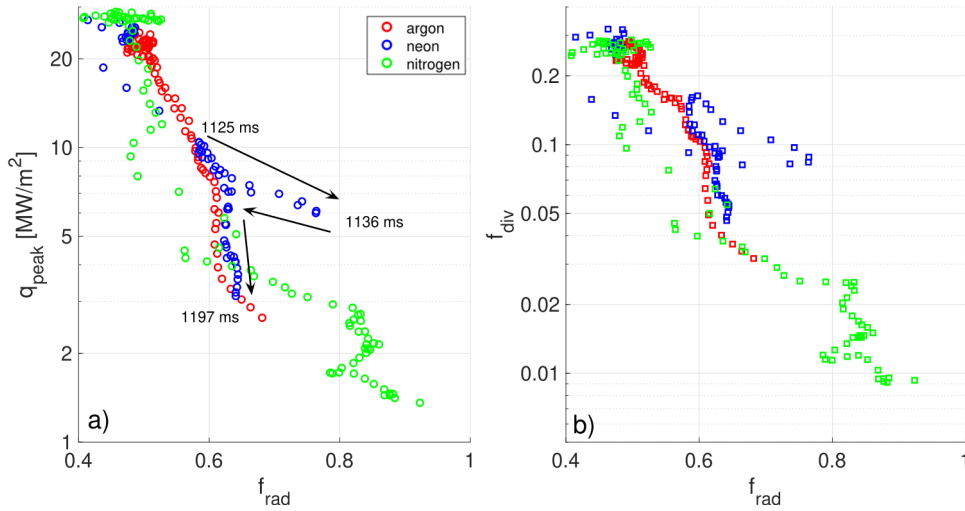


Figure 2.7: Dependence of generic divertor heat flux parameters q_{peak} and f_{div} on the radiated fraction f_{rad} for discharges with argon (#19087), neon (#19097) and nitrogen (#15977) seeding. Published in [17].

It is clear that nitrogen seeded experiments allow the most to reduce the incoming fluxes to the divertor. In this thesis, we therefore focused on discharges obtained during nitrogen experiments.

The measured spectrum from the nitrogen seeding detachment experiment could be seen in Fig. 2.8a with spectrometer field of view in Fig. 2.8b. Nitrogen lines could be identified mainly near UV to blue spectrum, with one line near the green colour wavelength. Therefore, the nitrogen radiation are mostly visible on the blue pixels of the colour cameras, as well as on the green ones. However, the red pixels are also sensitive in the blue region of the visible spectrum and also catches the nitrogen detachment front. This can be especially useful when both blue and green components are saturated.

One interesting point while studying detachment is where the radiation occurs and how it is distributed. This is where tomography yields interesting results and this is the aim of this thesis.

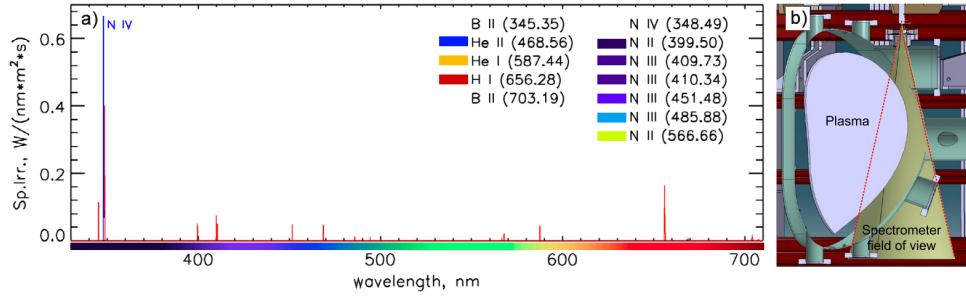


Figure 2.8: Nitrogen lines identified in the measured spectrum in discharge #15976 at $t = 1150\text{ms}$ (a) and the field of view of the minispectrometers (b). Edited images taken from [16].

2.4 Forward and reversed field detachment discharges

From whole detachment campaign on the COMPASS tokamak and many potential discharges to study, two were chosen - forward fields discharge number 15977 and reversed fields discharge number 20919. Some of the basic parameters of these discharges can be seen in Fig. 2.9 - for forward fields #15977, in Fig. 2.9a and for reversed fields #20919 in Fig. 2.9b.

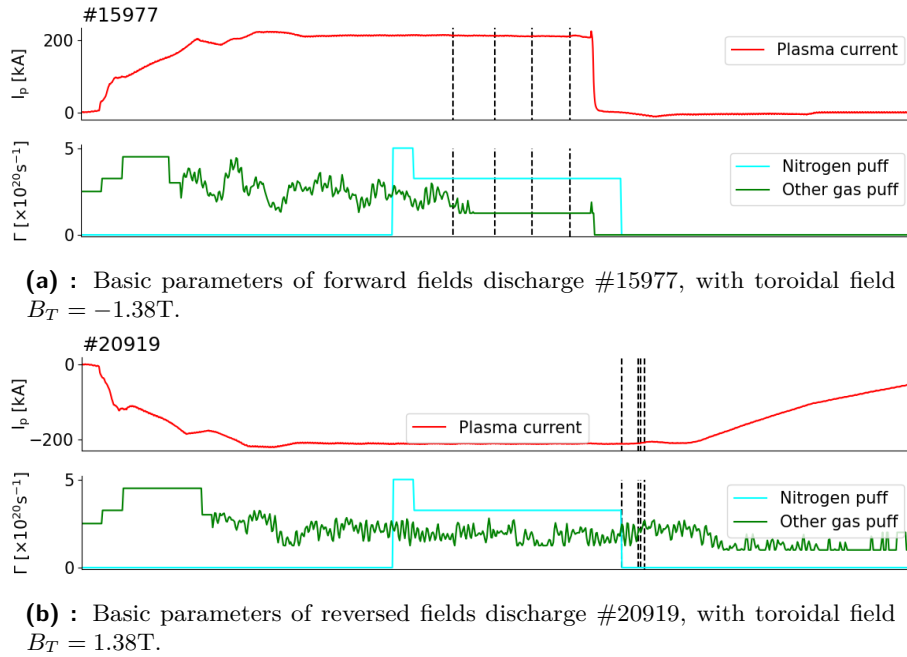


Figure 2.9: Parameters of forward fields discharge #15977 and reversed fields discharge #20919. Black dashed lines mark times of the images taken by RIS cameras in Fig. 2.11 (forward fields) and Fig. 2.12 (reversed fields).

The only difference between these two discharges was the direction of the electric and magnetic fields, which was reversed in #20919. Otherwise

plasma cross section and plasma density were identical, as well as the nitrogen injection.

These particular discharges were chosen because a study was underway in this area and the results of this work could be used subsequently. The optimal choice of discharge number was the ones that had the most symmetrical structures that were most visible in the images taken by the RIS cameras. Nevertheless, most of detachment discharges with similar parameters behaved alike, so the choice of the number of discharges was partially arbitrary.

Chosen RIS camera views from respective discharges can be seen in Fig. 2.11 and Fig. 2.12. From the figures, it is evident that the direction of fields had impact on the detachment. In both cases, nitrogen first propagated toroidally from the location of puff. However, the resulting radiation patterns then varied and occurred at different stages of seeding.

The nitrogen radiation in forward fields discharge #15977 occurs mainly around the X-point, shifting from high field side (HFS) to the low field side (LFS). It can be seen, from the video of the discharge, that the radiation pattern moves upwards and to the LFS and oscillates. At some point, it triggers a disruption and the discharge terminates.

During the reversed fields discharge #20919, the nitrogen radiation is located at three different location. First the radiation seems to be localised in the HFS for a majority of time, but then it elongates along separatrix (or magnetic flux surface) towards the top of the chamber. This elongation is very fast lasting 3 ms. Radiation then seems to be steadily focused on the top of the vacuum chamber.

These different pattern behaviours are likely caused by plasma drifts that are different for reversed and forward fields [18], see in Fig. 2.10 some of the drifts. The exact role of drifts on the detachment is the subject of actual simulation studies (SOLPS and SOL-edge). To verify the results of these simulations, real measured data are needed for comparison. The results presented in this thesis are intended to be used for comparison with simulations.

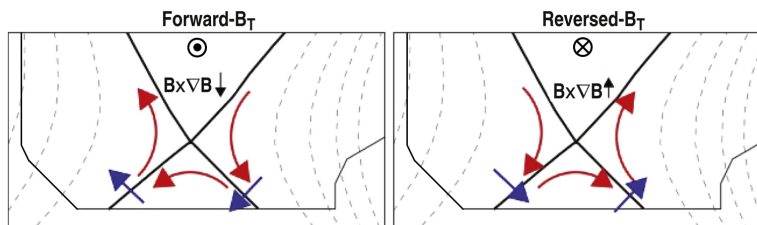
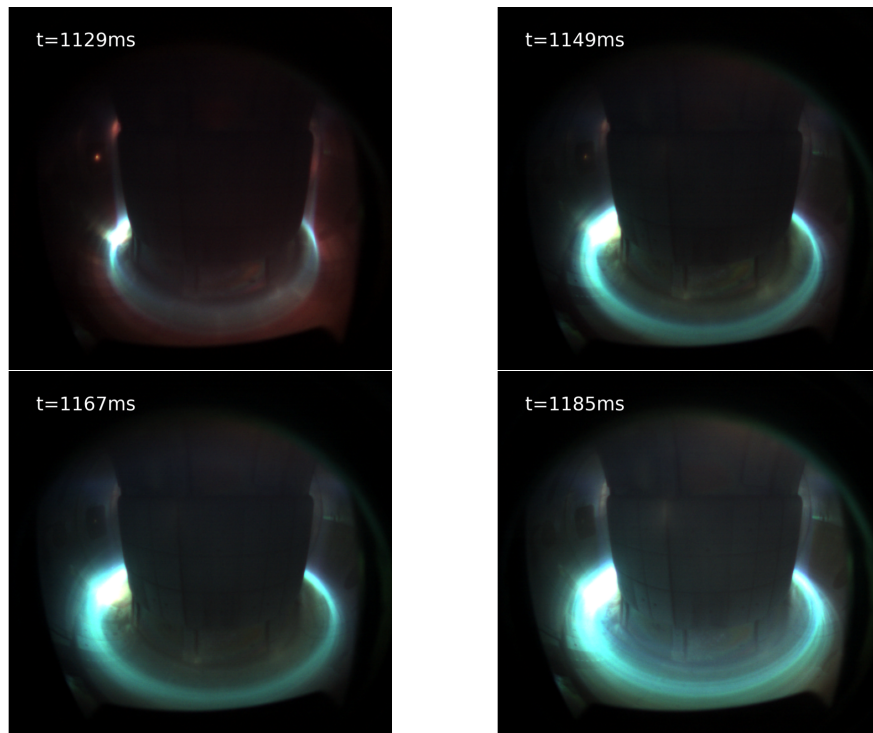
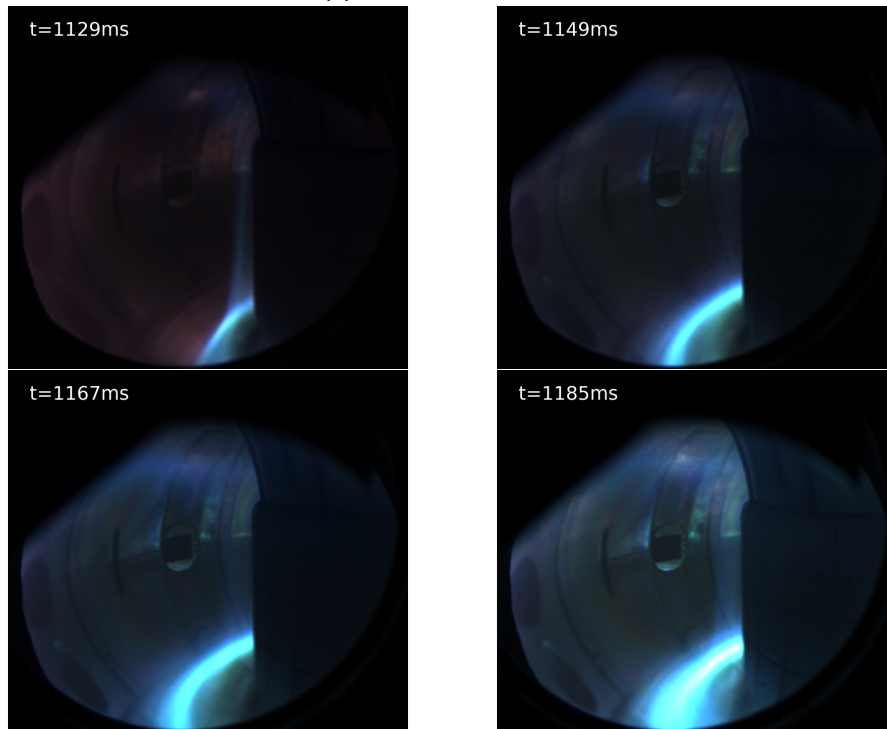


Figure 2.10: The plasma $E \times B$ drifts for both directions of the toroidal field. The poloidal drifts driven by radial gradients in T_e are shown in red. The radial drifts driven by poloidal gradients in T_e are shown in blue. Edited image taken from [18].

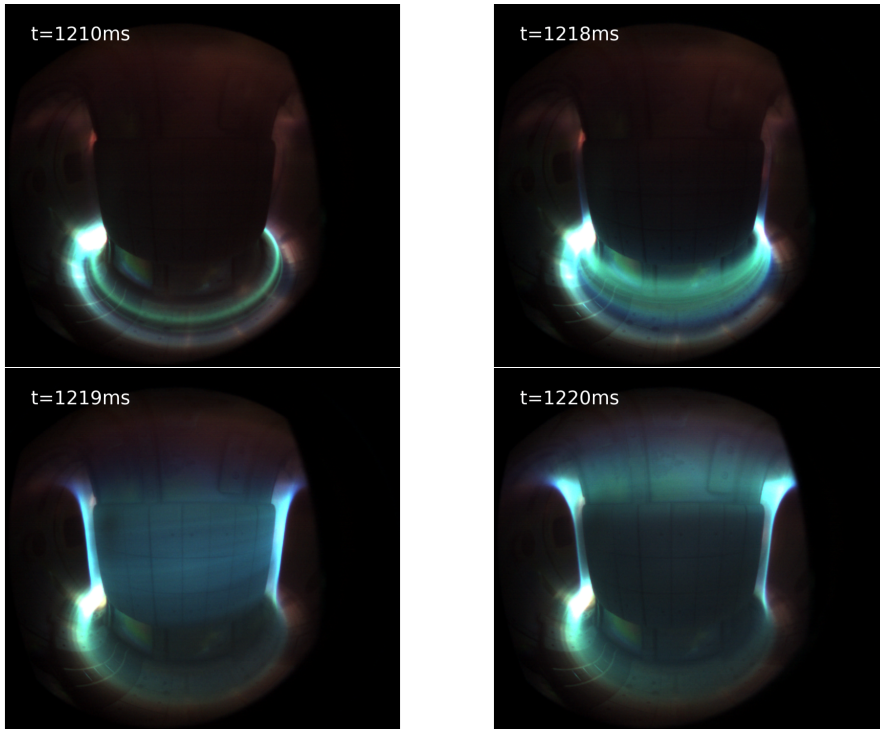


(a) : RIS1 camera view

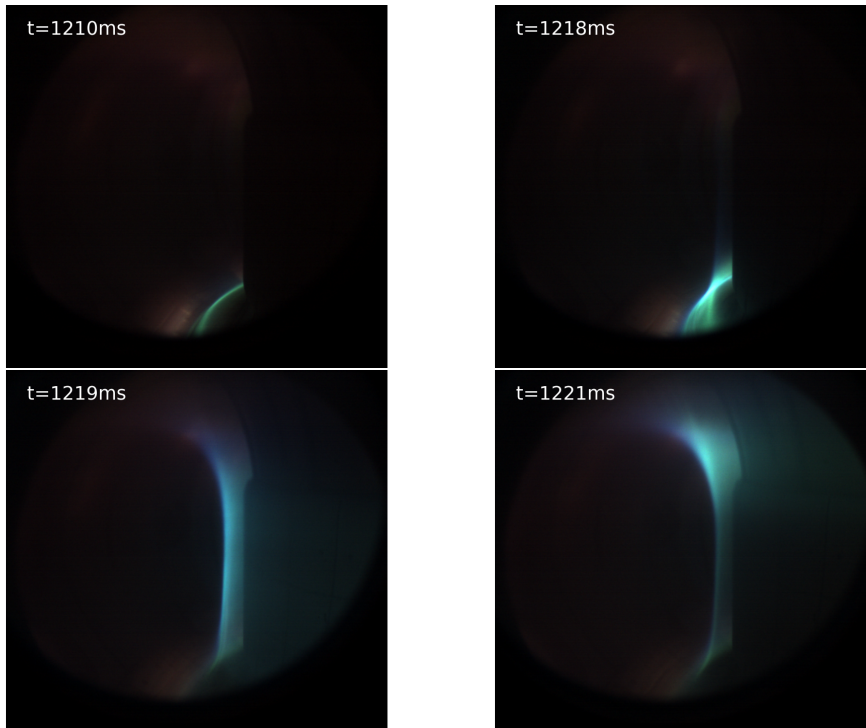


(b) : RIS2 camera view

Figure 2.11: Different plasma patterns of nitrogen radiation during discharge #15977 captured by RIS1 and RIS2 cameras.



(a) : RIS1 camera view



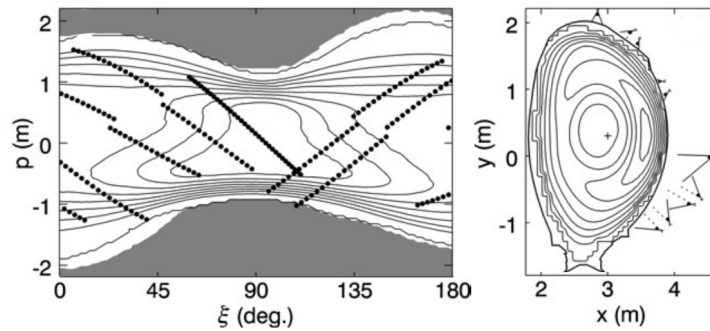
(b) : RIS2 camera view

Figure 2.12: Different plasma patterns of nitrogen radiation during discharge #20919 captured by RIS1 and RIS2 cameras.

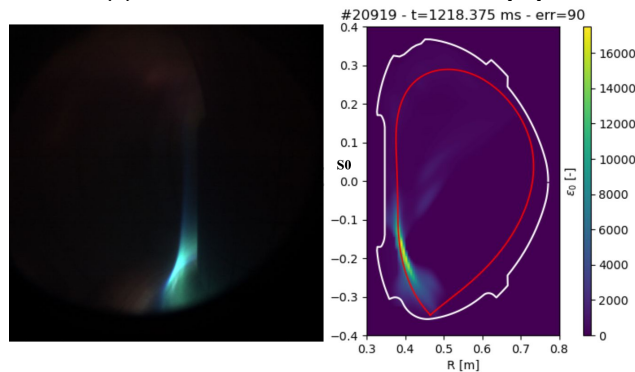
Chapter 3

Procedure for camera tomography of tokamak plasmas

Tomography is already widely used in fusion research as a plasma diagnostic [19]. The data collected from the measurements for tomography are usually obtained from linear systems, but there exist other array systems as seen in Fig. 3.1.



(a) : Bolometry tomography at JET [11]



(b) : Tomography of camera data at COMPASS.

Figure 3.1: Examples of projected data obtained from measurements (left) by different systems, with corresponding tomographic reconstructions (right). Bolometry is a linear system (a) and camera is an array system (b).

This thesis focuses on the single camera observation, which limits the measured data to the visible spectrum and provides large number of measured

values to work with.

But before performing the analysis and tomographic inversion, it is needed to approximate and model the camera view, so that the data could be properly processed. This will be topic of the following section. Other sections will focus on the other steps during tomographic inversion.

3.1 Camera view calibration

In order to map the actual field of view of the chamber, it is essential to model the camera view. This model allows describing where and how the measured light is collected. However, the resulting captured image by RIS cameras records light that has passed through many optical elements before reaching the camera chip plane, making the exact description of its path very complex. That is why an approximation by a pinhole camera is made, in which the whole camera apparatus with all optical devices is approximated by a screen collecting the light passing through an infinitely small pinhole [20].

The calibration and approximation is performed using the Calcam software [20]. Calcam has a feature for calibrating the camera view called "point fitting", where the user identifies matching positions between a camera image and a CAD model of the scene viewed by the camera, in order to fit a pinhole model for the camera geometry. Fig. 3.2 shows how this "point fitting" calibration is performed.

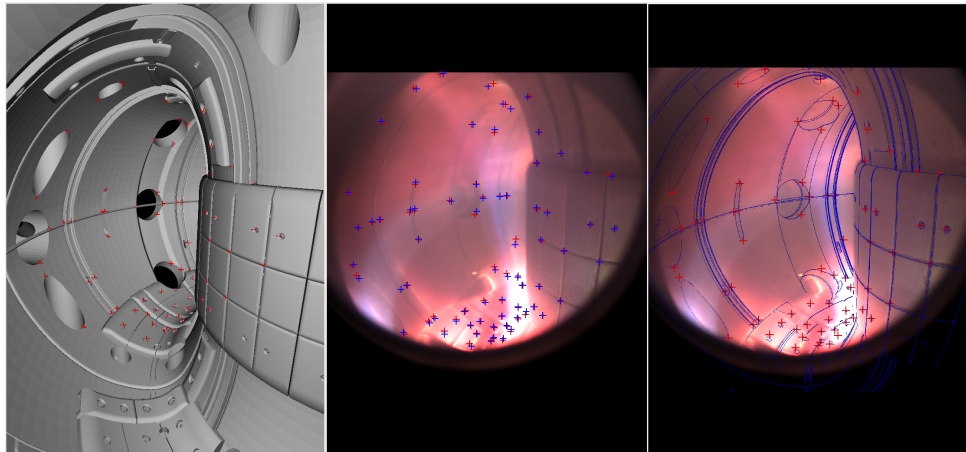


Figure 3.2: Screenshots from Calcam point fitting calibration, where user identifies points in CAD model (left) with captured image (middle), so that CAD view and image overlap each other (right). User-identified points are represented by red crosses, while fitted points and the CAD wireframe are represented by blue crosses and lines.

Usually the camera images provided for calibration are taken before discharges with specifically illuminated chamber for this purpose. However, for

the discharges analysed in this thesis there were no such images. Therefore images taken during the discharges were used. Moreover, there were cases where some parts of the CAD model did not exactly match the configuration in the vessel because some divertor plates were changed, but no such model was available. Therefore, point fitting could not be realised for this part of the view.

Another feature that can improve quality of the camera model is the so called chessboard calibration. It helps to model distortions caused by optics, detecting the edges of chessboard squares of known size and numbers at different distance and angles. However, for the images used in this thesis, this calibration was unavailable.

The calibration results provide pinhole camera model, which contain information about the pupil position and Lines Of Sight (LOS). Example of modelled view with lines of sight, which are limited by the boundaries of the chamber, is shown in the Fig. 3.3.

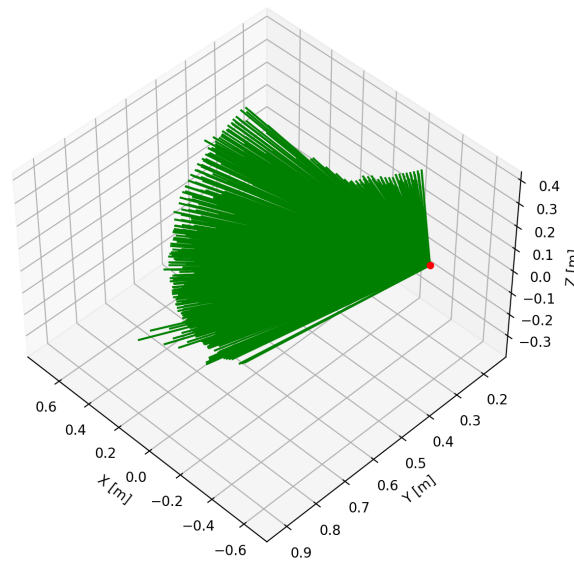


Figure 3.3: Plotted lines of sight (green) and camera position (red) of the RIS2 camera from Calcam calibration in Cartesian coordinates. In Calcam model, there is one line of sight per pixel generated - 788480 lines are displayed in this figure. Calibration for RIS2 camera from discharge #20919 was used.

3.2 Tomography of single camera observation

Here, the tomography principle of single camera observation is described. For this purpose, images recorded by fast visible cameras are used for the tomographic inversion. An example of such system are the two RIS cameras installed at COMPASS. They measure non calibrated line-integrated light

I_0 along lines of sight, from which the emissivity function S_0 could be retrieved, after approximating the whole camera apparatus by a pinhole camera.

Let $S_0(\psi, \theta, \varphi)$ be the plasma emissivity at a point M characterised by its field line coordinates (ψ, θ, φ) , where ψ is a flux coordinate, θ a poloidal coordinate and φ the toroidal angle. Assuming that radiation is isotropic and that the plasma is transparent, the intensity collected by the camera at the pixel (x, y) is given as:

$$I_0(x, y) = \int_{p_c}^{+\infty} S_0(\psi(s_{xy}), \theta(s_{xy}), \varphi(s_{xy})) ds_{xy} + \eta \quad (3.1)$$

where (x, y) are the horizontal and vertical coordinates in the image plane, s_{xy} is the curvilinear abscissa along the ray passing through (x, y) (i.e. line of sight), p_c the position of the pupil on the ray and η is an additive term to account for other contributions to the measured data (noise, reflections or errors).

In principle, the emissivity $S_0(\psi, \theta, \varphi)$ could be retrieved from Eq. 3.1. However, the camera is observing a 3D object projected onto the 2D chip plane and there is a lack of information in one direction, with no existing mapping. The solution to this dimensional mismatch is found in the assumption of toroidal symmetry of the observed objects. This eliminates the toroidal angle dependence of emissivity in Eq. 3.1 to $S_0(\psi(s_{xy}), \theta(s_{xy}))$, which now depends on two coordinates only. The crossing of the lines of sight in their projections on the poloidal plane allowing the use of tomography. An illustration of the imposed requirements is given in Fig. 3.4.

Even though the inversion problem was simplified and possibly solvable, it is still complicated to inverse the emissivity S_0 from integral Eq. 3.1. That is why discretization, so that the integral problem would be transformed to matrix equation and numerically inverted.

For this purpose, methods implemented in a python package called Tomotok [21] were used. Majority of Tomotok package consists of inversions methods and framework easing computations of inversion for tokamak data. From this part of the thesis, most of the processes were done using this package, including discretization, geometry matrix creation, inversions and other minor functions.

3.3 Discretization and geometry matrix

The poloidal plane cross section on which the emissivity S_0 pattern will be reconstructed, is called the reference poloidal plane. To discretize the problem, both the camera image I_0 and reference poloidal plane have to be discretized. The image is already discretized by the pixels of the CCD sensor

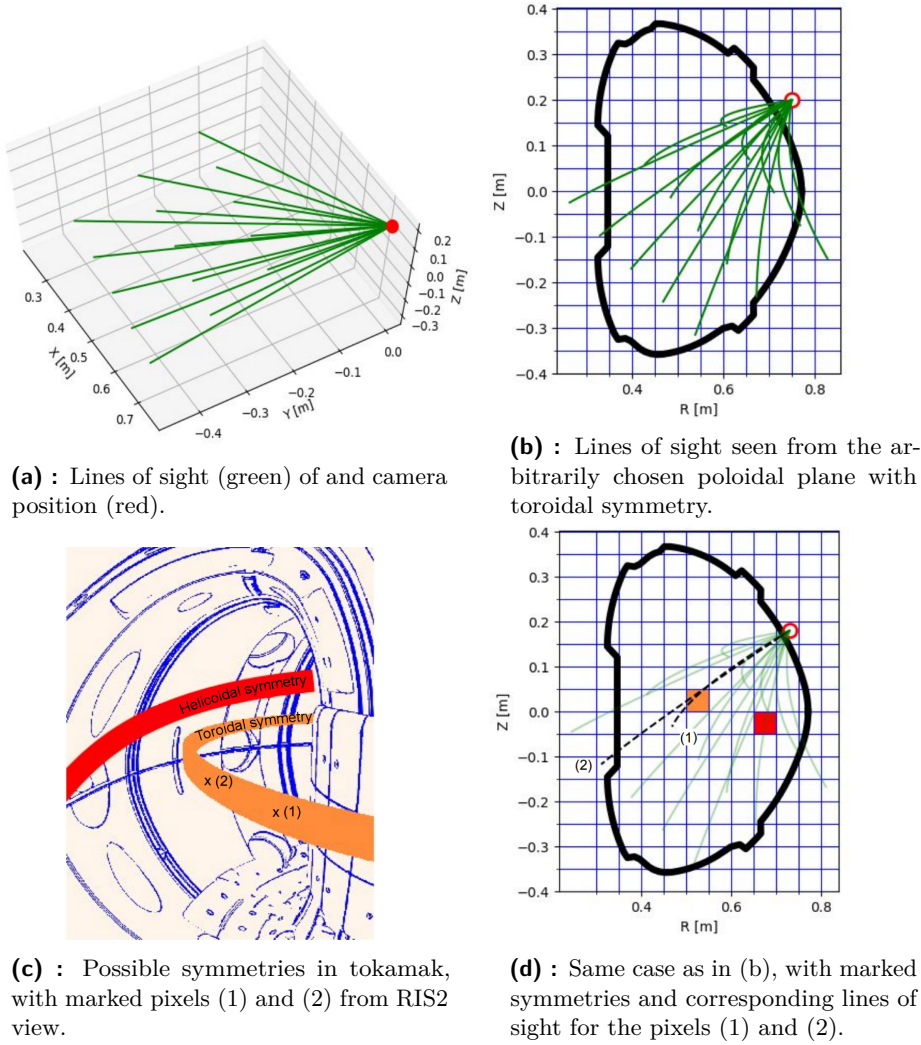


Figure 3.4: Illustrations to show relevance of symmetries and line of sight crossing. Image courtesy of J. Cavalier.

in the camera and the reference plane is discretized on a chosen mesh grid.

The second step is to transform the integral equation to a matrix equation. The matrix that allows this is called the geometric matrix (or transfer matrix, contribution matrix) denoted by \mathbf{T} . The justification for this transformation is as follows. From Eq. 3.1, we can assume that there is a linear mapping $\mathcal{T} : \mathbf{S}_0 \rightarrow \mathbf{I}_0$. This mapping connects the radiation patterns on the 2D reference plane mesh grid to the image of the captured 3D radiation structure, which follows toroidal symmetry. Because the emissivity reference plane (source set) and captured images (target set) are discretized, they are of finite dimensions (finite cells and pixels). Eq. 3.1 could therefore be written in the following matrix form:

$$\mathbf{I}_0 = \mathbf{T} \cdot \mathbf{S}_0 + \eta \quad (3.2)$$

where \mathbf{S}_0 is a column vector containing the emissivity of each cell of the reference plane mesh grid, \mathbf{I}_0 is a column vector containing intensity of each pixel measured by the CCD camera, \mathbf{T} is the matrix defining the linear mapping \mathcal{T} of emissivity \mathbf{S}_0 to the image \mathbf{I}_0 and η is again the additive term expressing the noise and reflections or any non symmetric features in general.

The process of discretization and creation of the geometric matrix \mathbf{T} in practice is described in detail in the following points:

- First step is to specify the poloidal reference plane, where the emissivity will be reconstructed. The position on poloidal plane is characterized by the distance to the main axis of tokamak R and height in the poloidal midplane z . Using these coordinates it is possible to define the boundaries of reconstructed area. The width of the reference plane is given by the minimum radius R_{\min} , which is closer to the central column, and the maximum radius R_{\max} , which is closer to the outer wall. The height is given by the minimum and maximum height z_{\min} and z_{\max} , which determine the bottom and top boundaries. After setting the boundaries, the reference poloidal plane is discretized on a regular rectangular grid, with specified grid resolution, given by the number of rows and columns. With these conditions, any mesh cell center G has coordinates (R_G, z_G) in a way that $R_{\min} < R_G < R_{\max}$ and $z_{\min} < z_G < z_{\max}$. The size and resolution of the grid can be adjusted as needed, and sometimes a grid other than rectangular can be created by selecting only certain cells for processing. In practice, higher resolution grids are also more computationally demanding.
- Finally, the geometric matrix \mathbf{T} can be obtained by numerical integration. In this thesis, function from Tomotok [21] was used for this purpose. The input data, the radial and vertical coordinates of the start and end points of LOS for each pixel, are obtained from the Calcam calibration (Fig. 3.3) with the defined mesh grid. The function first calculates the distance between the start and end points of LOS for each pixel. It then iterates over each LOS and divides it into smaller segments based on the step size, and for each segment it computes its radial distance R . 2D-histogram is then created, with the radial and vertical coordinates of the segments within the grid's radial and vertical borders, that mimics the mesh grid, with same bin (cell) sizes. Let now H_k be the value in the 2D-histogram, which is associated to an emissivity mesh grid cell S_{0_k} . One element of geometry matrix T_{ik} is then computed as:

$$T_{ik} = H_k \cdot (\text{step length}) \quad (3.3)$$

In the i^{th} iteration, one row of the matrix is obtained that describes the transformation of the emission pattern on the grid to a i^{th} pixel. Thus after iterating through all LOS associated to every pixel the geometry

matrix \mathbf{T} has following shape:

$$\begin{matrix} & \# \text{ mesh cells} \\ \# \text{ pixels} & \begin{pmatrix} t_{11} & \dots & t_{1k} \\ \vdots & \ddots & \vdots \\ t_{n1} & \dots & t_{nk} \end{pmatrix} \end{matrix} \quad (3.4)$$

allowing to write (3.2) as:

$$\begin{pmatrix} I_{0_1} \\ \vdots \\ I_{0_n} \end{pmatrix} = \begin{pmatrix} t_{11} & \dots & t_{1k} \\ \vdots & \ddots & \vdots \\ t_{n1} & \dots & t_{nk} \end{pmatrix} \cdot \begin{pmatrix} S_{0_1} \\ \vdots \\ S_{0_k} \end{pmatrix} + \eta \quad (3.5)$$

From now on, for simplicity of notation and description, the term η will be omitted, giving the final form of Eq. 3.5 as:

$$\mathbf{I}_0 = \mathbf{T} \cdot \mathbf{S}_0 \quad (3.6)$$

from which the emissivity \mathbf{S}_0 is extracted by inversion of the matrix \mathbf{T} . Visual example of Eq. 3.6 is shown in Fig. 3.5, where simple grid pattern of emissivity \mathbf{S}_0 is projected by the geometry matrix \mathbf{T} into the camera plane.

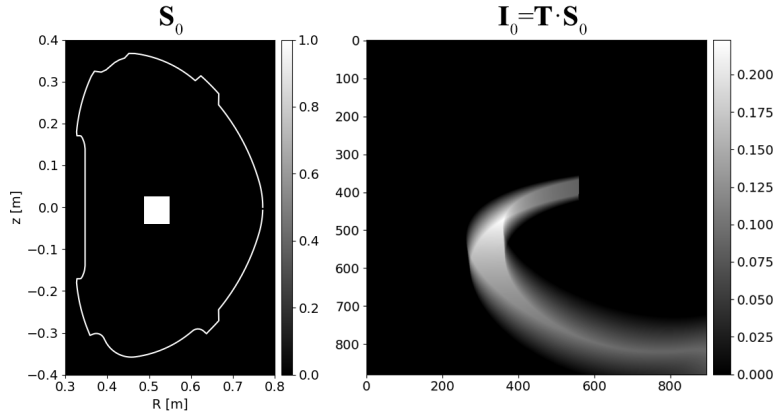


Figure 3.5: Example of projection of a simple grid poloidal plane pattern (left) into the image (right) using the geometric matrix \mathbf{T} . Geometry matrix \mathbf{T} for RIS2 camera from discharge #20919 was used.

3.4 Inversion algorithms

The final step in tomography is the inversion of Eq. 3.6. However, this task is ill-posed, which means that small errors can lead to serious errors in the reconstructed reference plane. Therefore, conventional inversion methods may not work and other specialized methods must be used, that are more robust for the inversion and can properly handle the errors η . These methods typically use regularization, which sets some reasonable assumptions, e.g.

some restriction on the result complexity (commonly enforcing smoothness of the result) [19]. Nevertheless, there are other methods that address this problem with different approaches.

Tomotok has three methods implemented - Minimum Fisher Regularization (MFR) [19, 22], BiOrthogonal Basis Decomposition (BoB) [23, 24] and Linear Algebraic Methods [25]. In this thesis MFR and BoB methods are used. Both methods are based on different principles, which will be introduced in the following subsections.

3.4.1 Minimum Fisher Regularization

This method is regularised, which allows to have fewer observations channels than the cells in the grid, making it flexible for application to visible camera data as well as AXUV data. The algorithm for this method is based on Tikhonov regularization, which solves the ill-posed problem of inversion and consists of two loops. The inner loop searches for the optimal regularization parameter by comparing the intermediate result found in one iteration with the signal. The outer loop regularises the problem using the optimal values of regularisation parameter found by the inner loop that determines the strength of a-priori information imposed by smoothing matrix. Since this method is based on intermediate results, it is classified as a nonlinear method [21].

As already mentioned, the method first uses Tikhonov regularization, which when applied to Eq. 3.6 gives:

$$\mathbf{T}^T \cdot \mathbf{I}_0 = (\mathbf{T}^T \cdot \mathbf{T} + \alpha \mathbf{H}) \cdot \mathbf{S}_0 \quad (3.7)$$

which can be inverted and solved for S_0 by outer loop:

$$(\mathbf{T}^T \cdot \mathbf{T} + \alpha \mathbf{H})^{-1} \cdot \mathbf{T}^T \cdot \mathbf{I}_0 = \mathbf{S}_0 \quad (3.8)$$

where α is the regularization parameter and \mathbf{H} is the regularization matrix computed as:

$$\mathbf{H} = c_1 \mathbf{D}_1^T \cdot \mathbf{w} \cdot \mathbf{D}_1 + c_2 \mathbf{D}_2^T \cdot \mathbf{w} \cdot \mathbf{D}_2 \quad (3.9)$$

where \mathbf{D}_1 , \mathbf{D}_2 are matrices of numerical derivatives along locally orthogonal directions, c_1 , c_2 anisotropy coefficients (sum of c_1 and c_2 should be equal to 1) and \mathbf{w} is a matrix with weights for individual cells. The elements of the weight matrix are computed from the intermediate result $\mathbf{S}_{0\text{int}}$ as $1/\mathbf{S}_{0\text{int}}$ for non-zero elements of $\mathbf{S}_{0\text{int}}$, otherwise the predefined value \mathbf{w}_{max} is used. The value of the regularisation parameter α is tested using Pearson χ^2 test given by:

$$\chi^2 = \frac{1}{N_c} \sum_i^{N_c} \left(\frac{(\mathbf{I}_0 - \mathbf{T} \cdot \mathbf{S}_0)_i}{\sigma_i} \right)^2 \quad (3.10)$$

\mathbf{M}^T denotes transpose

\mathbf{M}^{-1} denotes inverse

where N_c is the number of pixels and σ_i is estimated noise measured by i^{th} pixel I_{0_i} . The optimal value is one, indicating that the reconstruction error is approximately equal to the estimated error of the measured data. The optimal value of the regularisation parameter from the test is then used to update the regularisation matrix and the inner loop repeats until the maximum number of outer cycles is reached [21]. Simplified workflow diagram of possible implementation algorithm is shown in Fig. 3.6. This method reconstructs a single emission plane from a single image, making it more challenging to reconstruct a larger number of images using MFR.

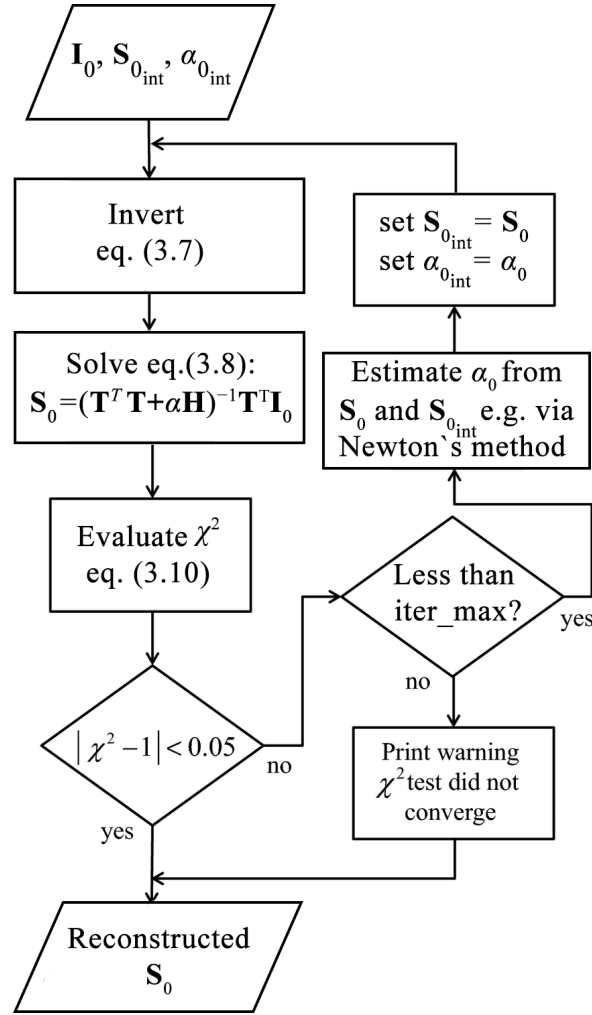


Figure 3.6: Simplified flowchart showing possible implementation of MFR algorithm, with defined convergence threshold of the Pearson's test. Edited image taken from [19].

3.4.2 Biorthogonal basis decomposition

This method solves the ill-posed problem without using the regularization. Consequently, it requires the number of collecting data channels (pixels) to

be larger (or equal) than the number of cells in mesh grid [26], i.e. the task has to be over determined [21]. BoB is therefore not suitable for systems composed of linear detectors (e.g. bolometers), where the number of channels is significantly lower. However, it is well suited to matrix camera systems, that are used in this thesis (RIS).

The great advantage of this method is that after performing the matrix decomposition, a simple inversion can be performed and all results can be obtained by simply multiplying the matrices with the images. Another feature is thresholding (see [23, 24] for more information), which keeps cells that contribute above a given threshold only and set the other ones to zero.

The core of the algorithm is to use biorthogonal dual basis set in the image space. Let $(\psi_\lambda)_{\lambda \in [1, \dots, N_\lambda]} = \{\psi_1, \dots, \psi_{N_\lambda}\}$ be an orthonormal basis of the reference poloidal plane mesh, of size N_λ , which is the number of cells on the mesh in the reference poloidal plane whose image on the camera is non-zero. Using this basis, emissivity \mathbf{S}_0 could be written as:

$$\mathbf{S}_0 = \sum_{\lambda=1}^{N_\lambda} s_\lambda \psi_\lambda = \sum_{\lambda=1}^{N_\lambda} (\psi_\lambda \cdot \mathbf{S}_0) \cdot \psi_\lambda \quad (3.11)$$

where s_λ are unknown constants. Eq. 3.6 then could be written as:

$$\mathbf{I}_0 = \mathbf{T} \cdot \mathbf{S}_0 = \sum_{\lambda=1}^{N_\lambda} s_\lambda \mathbf{T} \cdot \psi_\lambda \quad (3.12)$$

where $\mathbf{T}\psi_\lambda$ is the matrix containing the intensity of each pixel related to the image on the camera of the basis vector of the reference poloidal plane ψ_λ . If the coefficients s_λ could be found, the emissivity S_0 in the reference plane could be recovered. To do this, the adjoint basis of $(\mathbf{T}\psi_\lambda)_{\lambda \in [1, \dots, N_\lambda]}$ is used.

Assuming that \mathbf{T} is invertible, and using the relation given by the property of adjoint matrices:

$$(\mathbf{T} \cdot \mathbf{a}) \cdot \mathbf{b} = (\mathbf{a} \cdot \mathbf{T}^*) \cdot \mathbf{b} \quad (3.13)$$

it is possible to write following system:

$$\begin{aligned} \mathbf{T} \cdot \psi_\lambda &= \kappa_\lambda \cdot \chi_\lambda \\ \mathbf{T}^* \cdot \xi_\lambda &= \kappa_\lambda \cdot \psi_\lambda \end{aligned} \quad (3.14)$$

where $(\xi_\lambda)_{\lambda \in [1, \dots, N_\lambda]}$ and $(\chi_\lambda)_{\lambda \in [1, \dots, N_\lambda]}$ are two basis in the camera image plane (with \mathbf{T} being invertible) and κ_λ are chosen such that the ξ_λ are normalized ($|\xi_\lambda| = 1$) for all λ . Simplified visual example of vectors ψ_λ , χ_λ and ξ_λ is shown in Fig. 3.7.

Using Eq. 3.11, Eq. 3.13 and Eq. 3.14 emissivity \mathbf{S}_0 can be expressed as:

\mathbf{M}^* denotes adjugate of a matrix \mathbf{M}

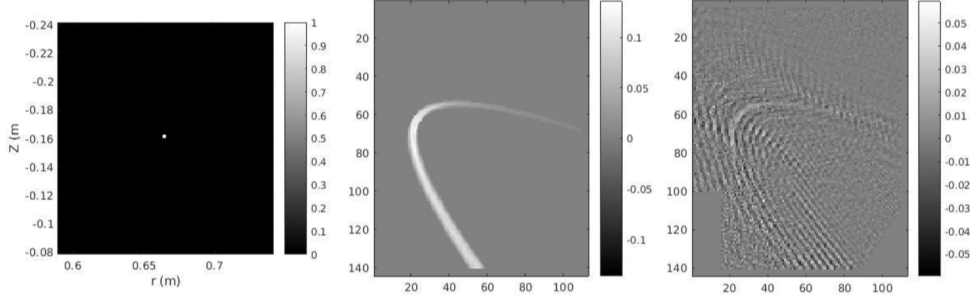


Figure 3.7: One example of a base vector ψ_λ (a single grid node) in the reference poloidal plane (left) and of the corresponding χ_λ (middle) and ξ_λ (right) families in the image plane. A different camera position was used for this image than the one presented in this thesis. Image taken from [23].

$$\begin{aligned}
 \mathbf{S}_0 &= \sum_{\lambda=1}^{N_\lambda} s_\lambda \psi_\lambda = \sum_{\lambda=1}^{N_\lambda} (\psi_\lambda \cdot \mathbf{S}_0) \cdot \psi_\lambda \\
 &= \sum_{\lambda=1}^{N_\lambda} \frac{1}{\kappa_\lambda} ((\mathbf{T}^* \cdot \xi_\lambda) \cdot \mathbf{S}_0) \cdot \psi_\lambda = \sum_{\lambda=1}^{N_\lambda} \frac{1}{\kappa_\lambda} (\xi_\lambda \cdot (\mathbf{T} \cdot \mathbf{S}_0)) \cdot \psi_\lambda \quad (3.15) \\
 &= \sum_{\lambda=1}^{N_\lambda} \frac{1}{\kappa_\lambda} (\xi_\lambda \cdot \mathbf{I}_0) \cdot \psi_\lambda.
 \end{aligned}$$

The coefficients s_λ could be then derived from Eq. 3.15, by comparing first and last line, as:

$$s_\lambda = (\xi_\lambda \cdot \mathbf{I}_0) \frac{1}{\kappa_\lambda} \quad (3.16)$$

where the only unknowns to be found are the ξ_λ .

To obtain the ξ_λ , the following cross product using Eq. 3.14 can be derived:

$$\begin{aligned}
 \forall(\lambda, \lambda') : \xi_\lambda \cdot \chi_{\lambda'} &= \frac{1}{\kappa_{\lambda'}} \xi_\lambda \cdot (\mathbf{T} \cdot \psi_{\lambda'}) \\
 &= \frac{1}{\kappa_{\lambda'}} (\mathbf{T}^* \cdot \xi_\lambda) \cdot \psi_{\lambda'} \quad (3.17) \\
 &= \frac{\kappa_\lambda}{\kappa_{\lambda'}} \psi_\lambda \cdot \psi_{\lambda'} = \begin{cases} 1 & \text{if } \lambda = \lambda' \\ 0 & \text{if } \lambda \neq \lambda' \end{cases}
 \end{aligned}$$

as vectors from $(\psi_\lambda)_{\lambda \in [1, \dots, N_\lambda]}$ form an orthonormal basis. Solving Eq. 3.17 yields ξ_λ , which can then be used in Eq. 3.15 to obtain the final result. To solve Eq. 3.17, projection of ξ_λ on the χ_λ basis (it is a basis of the image plane since ψ_λ is a basis of the poloidal plane and \mathbf{T} is invertible) is made, giving:

$$\xi_\lambda = \sum_{n=1}^{N_\lambda} C(\lambda, n) \chi_n \quad (3.18)$$

If the projection is performed for all N_λ vectors ξ_λ , in each projection having N_λ coefficients $C(\lambda, \cdot)$, $N_\lambda \times N_\lambda$ of coefficients are needed. If the projection in Eq. 3.17 is applied, the final system to be solved is:

$$\xi_\lambda = \begin{cases} 1 & \text{if } \lambda = \lambda' \\ 0 & \text{if } \lambda \neq \lambda' \end{cases} = \sum_{n=1}^{N_\lambda} C(\lambda, n) (\chi_n \cdot \chi_{\lambda'}), \quad (3.19)$$

written in matrix form as:

$$\begin{pmatrix} (\chi_1 \cdot \chi_1) & (\chi_2 \cdot \chi_1) & \dots & (\chi_{N_\lambda} \cdot \chi_1) \\ (\chi_1 \cdot \chi_2) & (\chi_2 \cdot \chi_2) & \dots & \vdots \\ \vdots & \vdots & \ddots & \vdots \\ (\chi_1 \cdot \chi_{N_\lambda}) & (\chi_2 \cdot \chi_{N_\lambda}) & \dots & (\chi_{N_\lambda} \cdot \chi_{N_\lambda}) \end{pmatrix} \begin{pmatrix} C(1,1) & C(2,1) & \dots & C(N_\lambda,1) \\ C(1,2) & C(2,2) & \dots & \vdots \\ \vdots & \vdots & \ddots & \vdots \\ C(1,N_\lambda) & C(2,N_\lambda) & \dots & C(N_\lambda, N_\lambda) \end{pmatrix} = \mathbf{I} \quad (3.20)$$

where \mathbf{I} is the unit matrix.

For the resolution of Eq. 3.20, different numerical methods can be applied to find the solution. In Tomotok, the solution is found by least-square method (`numpy.linalg.lstsq` [27]).

While solving the system, small singular values may appear which cause the inversion to fail. It is possible to treat these values as a zero if their values are less than a given threshold, making the problem well-posed. It could be debated if this should be considered as a regularization parameter. However, it is still very different approach than in the MFR one.

Chapter 4

Issues and solutions for tomographic inversion of camera data

This chapter will discuss how the data were handled, some issues encountered during the study, their solutions and results from previous detachment tomography study on the COMPASS tokamak. To illustrate the outcome of tomography that will be discussed in this thesis, in Fig. 4.1 a representative example is presented. The outcome usually consists of four output visualisations, which are the reconstructed emissivity, retrofit, camera signal and error (signal-retrofit).

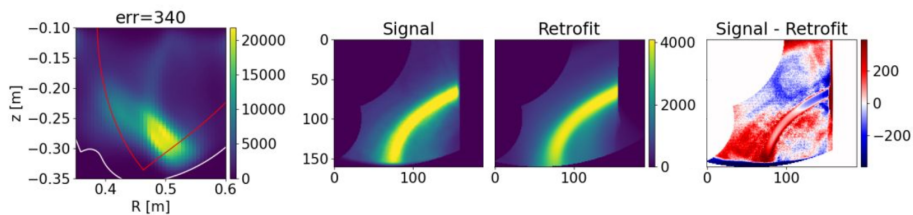


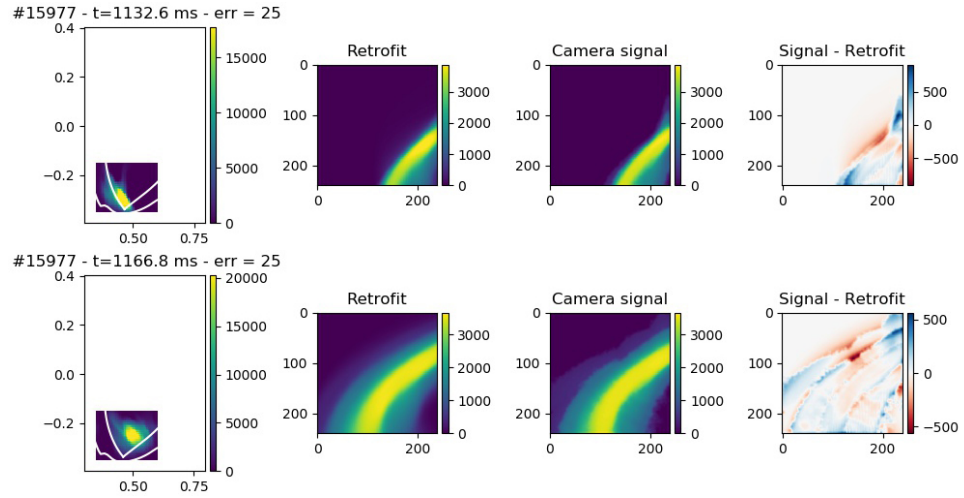
Figure 4.1: Example of a tomography result.

The emissivity figure is in this thesis displayed with the COMPASS chamber contour (white curve) and reconstructed separatrix (red curve) computed by EFIT code [28]. Retrofit, sometimes called forward model, is then obtained as a matrix product of the geometry matrix and reconstructed emissivity pattern (same as Fig. 3.5) and it shows the image the camera would see, if the emissivity of the reconstructed poloidal plane stands and assuming toroidal symmetry. Lastly, the difference between the signal and retrofit is an useful way to visualise the discrepancy between the results and input.

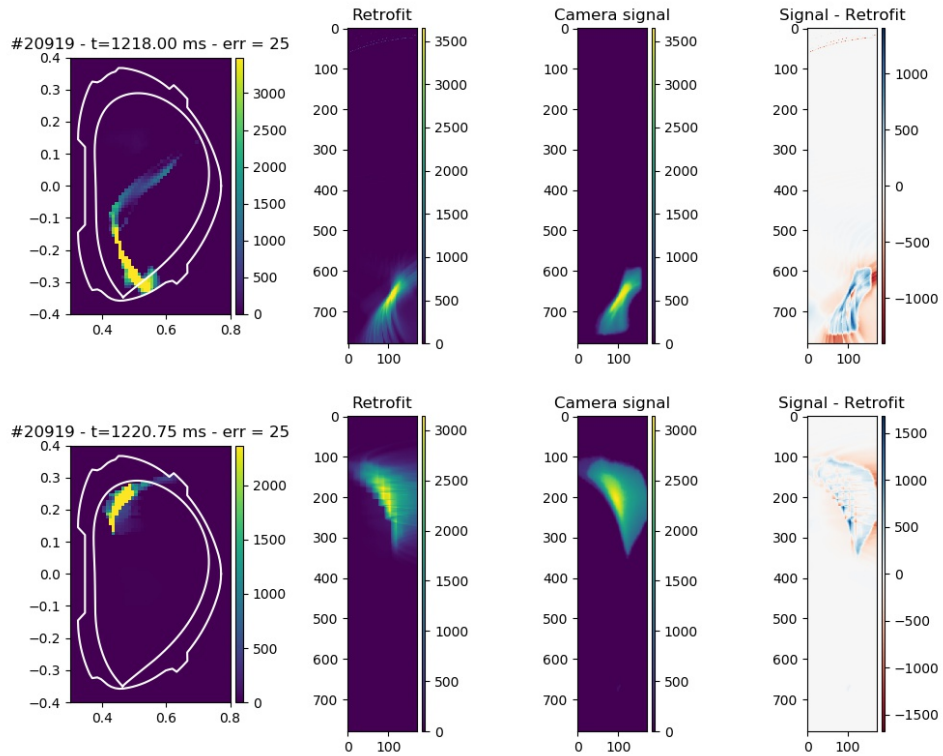
4.1 Preliminary analysis

A preliminary analysis on the topic of this thesis has been carried out by J. Cavalier in an internal communication [29]. In that case the tomographic inversion was performed for RIS2 views of discharges #15977 and #20919, using only MFR algorithm, the results of which can be seen in Fig. 4.2.

Approach also varied by using different regions for inversion or using Gaussian smoothing on the images [30] .



(a) : Reconstructions from discharge #15977.



(b) : Reconstructions from discharge #20919.

Figure 4.2: MFR inversions from the preliminary analysis [29].

The reconstruction of discharge #15977 in Fig. 4.2a showed that the radiation pattern was located mainly above the X-point, which is usually seen in detached regimes. However the reconstructed emissivity patterns in discharge #20919 in Fig. 4.2b did not match the physical expectations. It

was observed that the radiation pattern elongated from the X-point along the central column towards the top of the chamber. One notices the shift between the reconstructed emissivity and the LCFS, showing non-physical behavior, which indicates a flaw in the tomographic inversion. However, if this was the case, the reconstruction of discharge #15977 could also have been incorrect. It was therefore necessary to carry out a careful analysis of this matter again, which is the subject of this thesis.

1. First step in redoing the analysis was to make new camera calibrations. The comparisons between the new and old calibrations can be seen in Fig. 4.3. The new calibrations contained way more points for fitting, making them different in some areas, mainly near the central column and in the divertor, where the signal to be inverted is dominant.
2. Then to investigate the influence of the regularization, which could have caused the shift, MFR and BoB methods were used to cross-validate the results.
3. Lastly, a different selection of pixels used for inversion was implemented, as the reflections could have affected the results. The intention was to use only pixels that were observing the nitrogen structures in the processing, but at the same time, pixels that allowed the virtual intersection of LOS had to be taken into account. Therefore, areas affected by minor reflections were included as well.

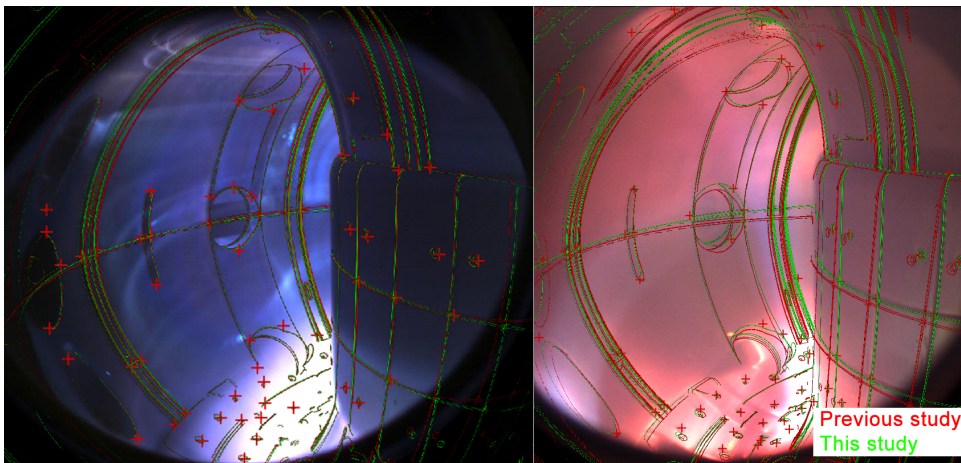


Figure 4.3: Comparison of the Calcam calibrations of discharges #15977 (left) and #20919 (right). The red wireframe represent the calibration used in the previous analysis and the green one represents the one used in this study.

4.2 Camera view selection

As mentioned before, the detachment experiments were observed by the two RIS1 and RIS2 cameras. The images of typical nitrogen structures from

toroidal symmetry of the signal. Thus the final image ready for tomographic inversion should be showing only areas where the nitrogen radiation occurs or areas with minor reflections.

In the #20919 discharge, the nitrogen radiation was located very close to the central column and the chamber reflected a lot of light, so the area used for the reconstruction was chosen in this respect. The pixels that were selected for the final reconstruction were in the areas where the radiation occurs, with part of the central column to allow a wider view without major reflections. The inclusion of the central column in the reconstruction mainly helped the MFR algorithm, where it facilitated error estimation. The resulting pixel selection is shown in Fig. 4.5, where the areas by which the selection was determined are also highlighted.

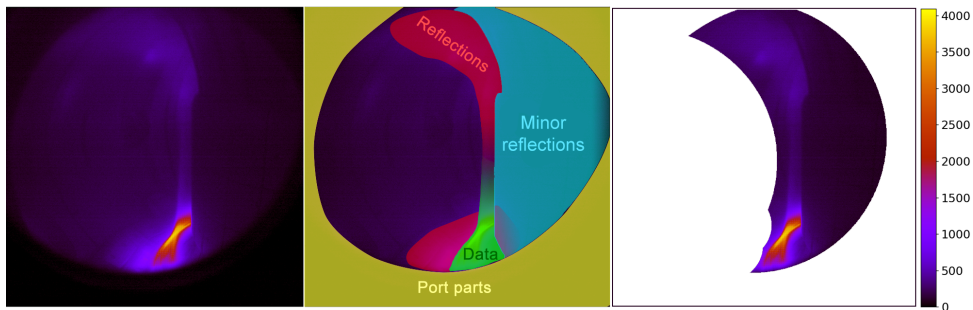


Figure 4.5: Pixel selection for discharge #20919. The left picture shows the raw image, the middle picture shows the marked areas, and the right picture shows the pixel selection after masking.

A somewhat different approach was used for discharge #15977, where reconstructions could be made for a relatively small area. This is mostly due to the fact that the radiation pattern stays close to the divertor region, only going slightly above the X-point. Therefore, only the region with nitrogen radiation was used, as shown in Fig. 4.6.

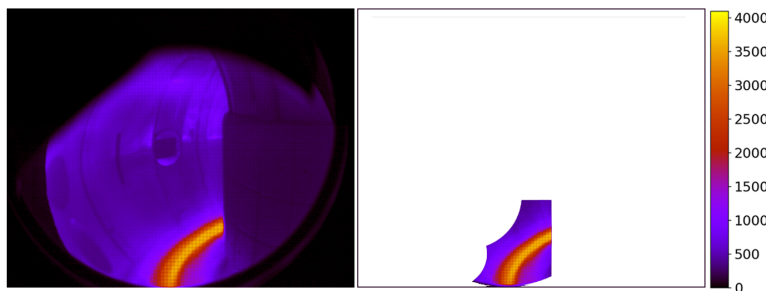


Figure 4.6: Pixel selection for discharge #15977. The left picture shows the raw image and the right picture shows the pixel selection after masking.

Overall the exact shapes and sizes of selected areas could differ a bit from what is shown in the figures, depending on the method, pattern and used mesh grid. However, it shows the general idea that was followed to obtain

Chapter 5

Tomography applied to the detachment experiments

In this chapter, the results of tomographic inversion applied on forward fields discharge #15977 and reversed fields discharge #20919 are presented. For both discharges, MFR and BoB inversion algorithms were used to cross-validate the results and study the effects of the regularization. The inversions were done for the entire time scale of nitrogen puff, but only six selected inversions describing the temporal evolution of nitrogen patterns are presented in this thesis for each discharge. Then to study the toroidal symmetry of the reconstructed nitrogen fronts, retrofit from RIS1 perspective was recreated using the emissivity in poloidal plane obtained from MFR inversions of RIS2, that was used to mimic RIS1 view, to see if the symmetry holds.

The resulting emissivity patterns mainly then describe the position of the radiation and not its exact values, since reflections were not taken into account in the reconstructions. There are methods that address this problem, but they were out of the scope of this thesis.

To avoid confusion, it is also good to point out that the reconstructed poloidal planes are oriented the other way around than the image (see results for reversed fields discharge, from which it is obvious).

The emissivity reconstructions presented in the next section were done using pixels of all colours of the image. However, comparing the reconstructions with the real image is better done using separate colours. This will be the topic of last section of this chapter, where the retrofits of MFR results are compared with real images.

5.1 Forward fields discharge #15977

The results of tomographic inversions for reversed fields discharge #15977 are shown in Fig. 5.1 and Fig. 5.2. When processing the data from this discharge, the reference grid and the area of the selected pixels were the same for both methods, as can be seen from the figures.

The reconstructed emissivity pattern was initially located along the sepa-

matrix on the HFS and then shifted towards the LFS above the X-point over time. After the detachment front reached the LFS, it started to shift back with an ascent towards the HFS. The detachment front then moves up more and more with some oscillations, until an instability (MARFE [31]) occurred and triggered the plasma disruption. The reconstruction seems to catch the behaviour that can be observed from the video by the naked eye.

However, in addition to the desired results, various artefacts caused by reflections, noise and inaccurate camera calibration also appear. For the MFR results, these artefacts appear as smoothed structures because of used regularization. Since BoB is a non-regularized method, reflections cause some non-physical values in the result in addition to the visible artefacts. Therefore, thresholding was applied to remove these values.

In the end the MFR and BoB algorithms produced qualitatively similar results, with minor differences.

5.2 Reversed fields discharge #20919

The results of the tomographic inversion for the reversed fields discharge #20919 are shown in Fig. 5.3 and Fig. 5.4. The used reference grid and the area of selected pixels for this discharge are different for the respective inversion methods. When the BoB method was applied to the same grid and pixels that were used for the MFR method, the operating memory was not sufficient to calculate the inversion. Thus, for the BoB method, a smaller grid had to be used which only covered the region of occurrence of the emissivity patterns. The selection of pixels was then done according to the retrofit, so that only the areas covered by the grid would be used.

The results of the MFR and BoB methods were again consistent. The reconstructed emissivity pattern was first located at the HFS along the separatrix. Then, within a few milliseconds, the pattern elongated along the central column and the maximum emissivity relocated to the top of the chamber closely following the separatrix. This pattern remained the same until the discharge termination. Thanks to the incorporation of new calibration and careful selection of pixels, the non physical shift observed in the preliminary study (see chapter 4) was not found here.

The artefacts caused by reflections are less visible than in previous discharge, probably because of pixel masking of the reflections. The MFR artefacts are smooth and have shapes following the path of LOS in the poloidal plane. With the BoB results, it can be seen that the artefacts are mainly concentrated around the edges of the grid. But thresholding again removed these undesirable values.

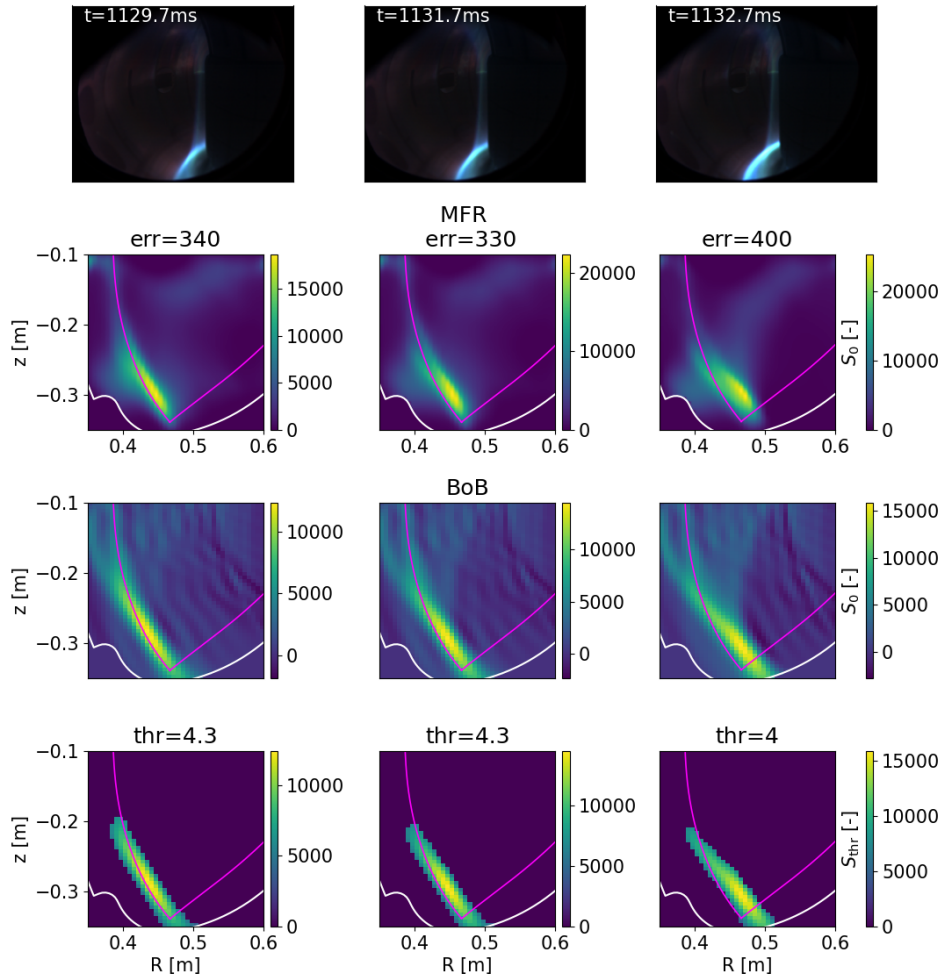


Figure 5.1: The first part of the tomographic inversion results for forward field discharge #15977. Figures in one column correspond to one time slice. First row of figures shows the raw images used for tomographic inversion, second row shows the emissivity reconstruction performed by the MFR algorithm with specified estimated error (err) and last two rows show emissivity reconstructions using the BoB algorithm with and without applied thresholding (thr), respectively.

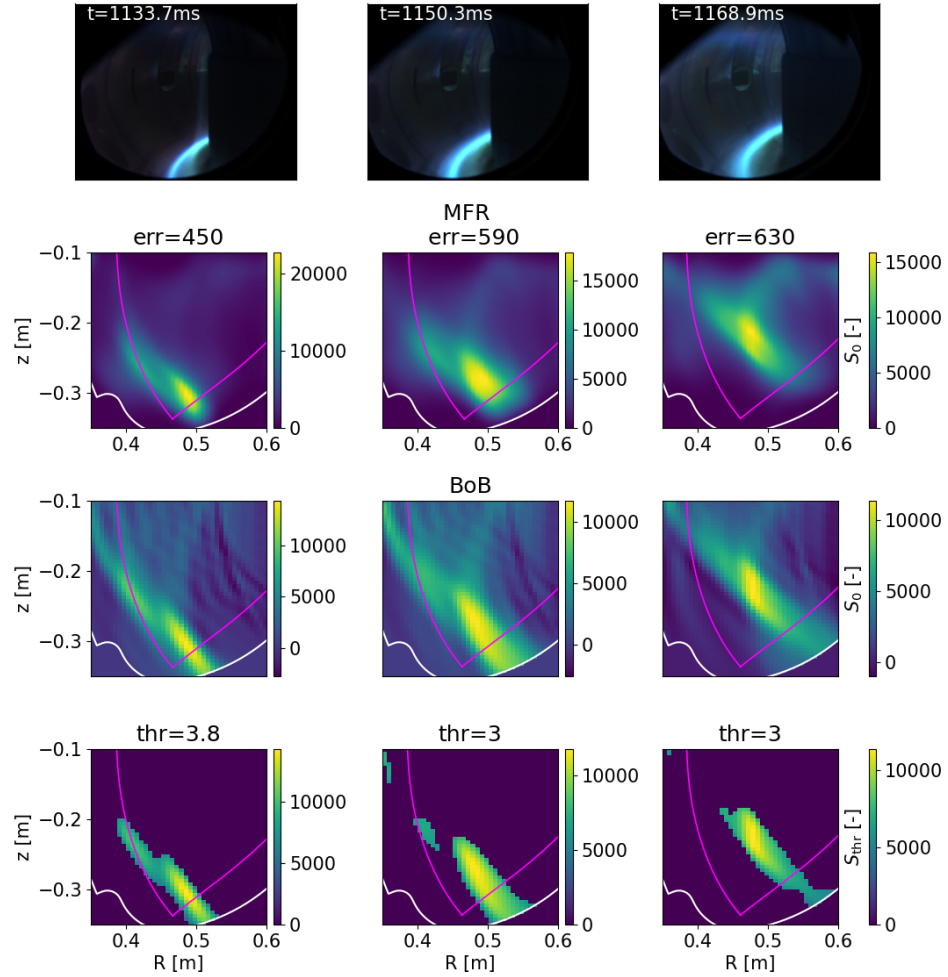


Figure 5.2: The second part of the tomographic inversion results for forward field discharge #15977. Figures in one column correspond to one time slice. First row of figures shows the images used for tomographic inversion, second row shows the emissivity reconstruction performed by the MFR algorithm with specified estimated error (err) and last two rows show emissivity reconstructions using the BoB algorithm with and without applied thresholding (thr), respectively.

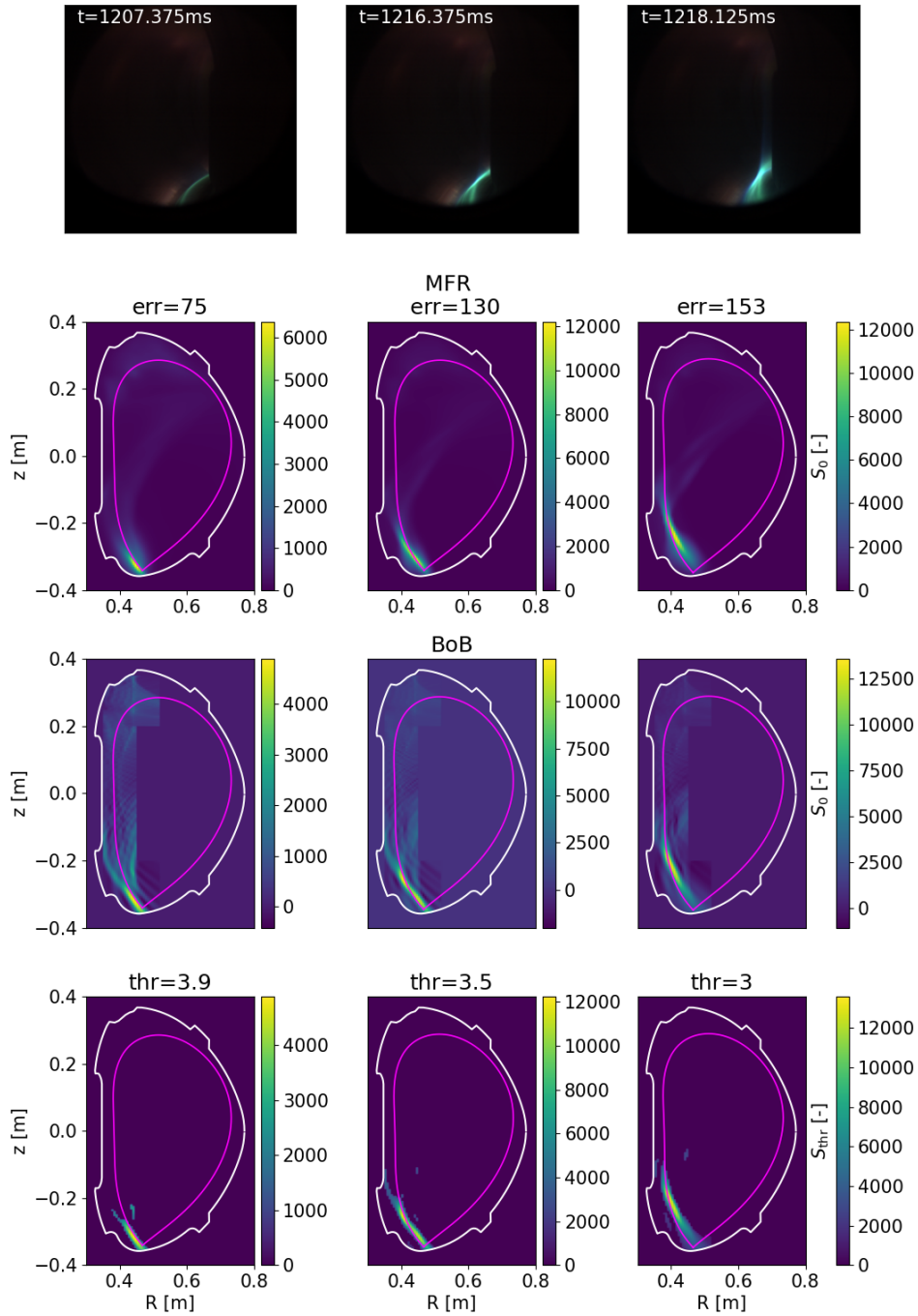


Figure 5.3: The first part of the tomographic inversion results for reversed field discharge #20919. Figures in one column correspond to one time slice. First row of figures shows the images used for tomographic inversion, second row shows the emissivity reconstruction performed by the MFR algorithm with specified estimated error (err) and last two rows show emissivity reconstructions using the BoB algorithm with and without applied thresholding (thr), respectively.

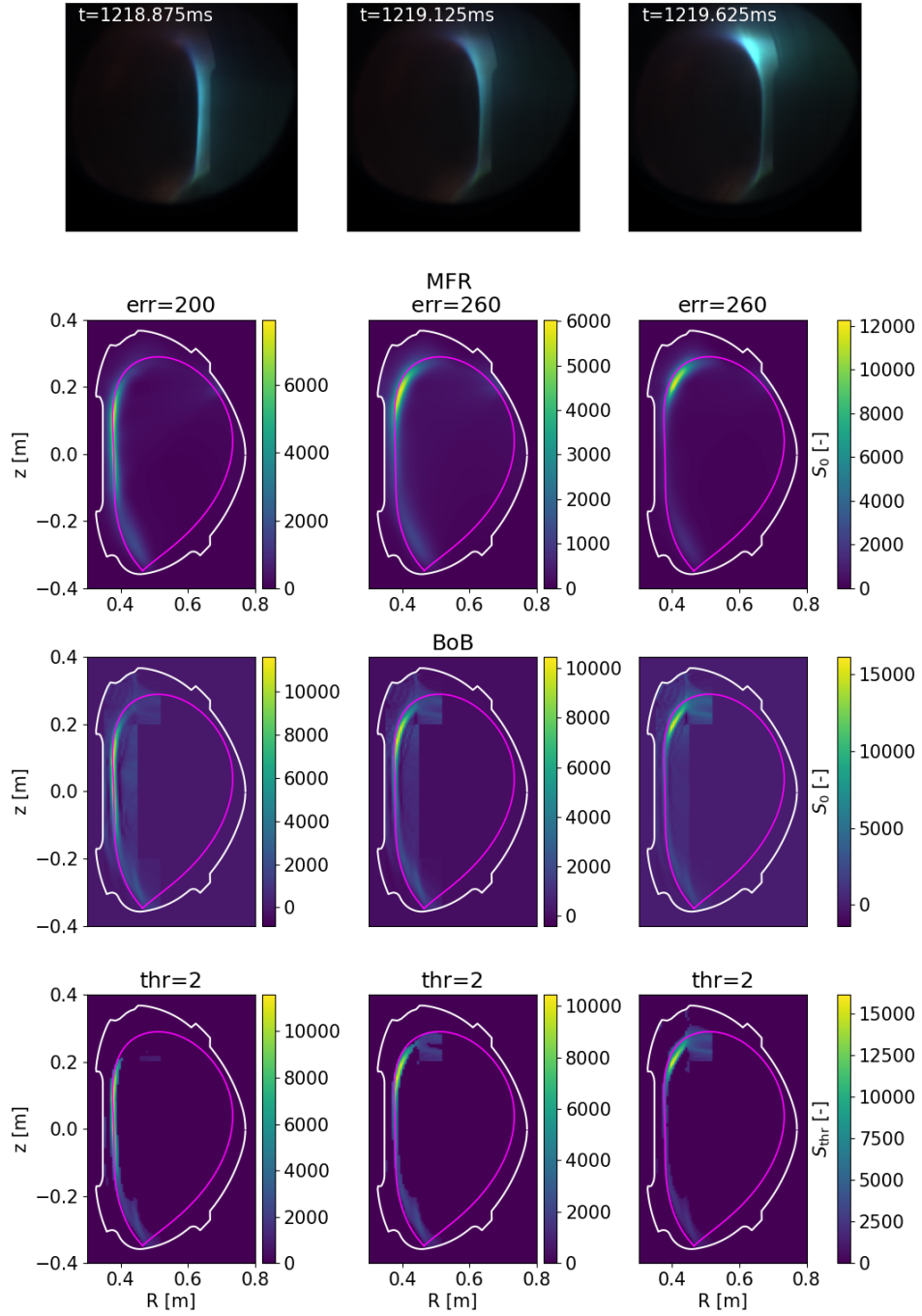


Figure 5.4: The second part of the tomographic inversion results for reversed field discharge #20919. Figures in one column correspond to one time slice. First row of figures shows the images used for tomographic inversion, second row shows the emissivity reconstruction performed by the MFR algorithm with specified estimated error (err) and last two rows show emissivity reconstructions using the BoB algorithm with and without applied thresholding (thr), respectively.

5.3 Toroidal symmetry investigation

The reconstructed RIS2 emissivity results may be used to create a retrofit constructed for other views than those from which the results were obtained, in particular, large views like the ones obtained with RIS1. This made it possible to discuss whether or not the reconstructed structures were toroidally symmetric and if the assumption made for tomography holds.

The RIS1 view is reconstructed by performing the product of the corresponding geometric matrix with the emission pattern. Here, the MFR reconstructions of only red pixels from RIS2 images were selected. MFR reconstructions were chosen over BoB because the resulting retrofit appeared smoother, allowing better comparison with the real image. However, this retrofit is not absolutely calibrated for all colours, meaning that comparison with an all colour image is inaccurate. It is possible to make four reconstructions for each colour in Bayer mosaic and use them to create four retrofits, where combining them creates artificial image for all colours, but an easier option is to analyse only one colour, as the comparison gives the same outcome. On top of it, the red colour was chosen because it had the lowest saturation among the colours captured by the RIS1 camera.

In addition, the positions where the RIS1 image pixels were saturated, were not included in the retrofit, because they are considered as deformed signals (their exact value is not known). Because of cameras not being absolutely calibrated, retrofits were scaled by a constant factor.

The comparison of retrofit and raw image signal was then given by absolute value of their difference and was normalised by the image signal. The pixels where the measured image signals were zero or saturated were ignored.

The resulting RIS1 retrofit of discharge #15977 can be seen in Fig. 5.5. Noticeably, the difference is to some extent toroidally symmetric, mainly in the zone of interest where the relevant signal is, shown by the cyan contour. However it seems, that the difference only follows the symmetry position wise and not in radiation magnitude. Additionally, towards the end of the injection (right figures), the symmetry seems to gradually deteriorate towards the toroidal direction of the nitrogen injection location.

The RIS1 retrofit of discharge #20919 is shown in Fig. 5.6. Here the symmetries holds only at the start of the injection (left figures) in a similar way as the case above. The nitrogen front then elongated to the top (right figures), where symmetries, specifically in the highlighted areas by cyan contour, were observed only on the side opposite if the nitrogen injection.

In general, the assumption of toroidal symmetry does not hold for large views like RIS1, as the gas injection appears to be quite localised toroidally. However, for narrower views, that are on the opposite site of the injection,

symmetry assumptions seem to hold well.

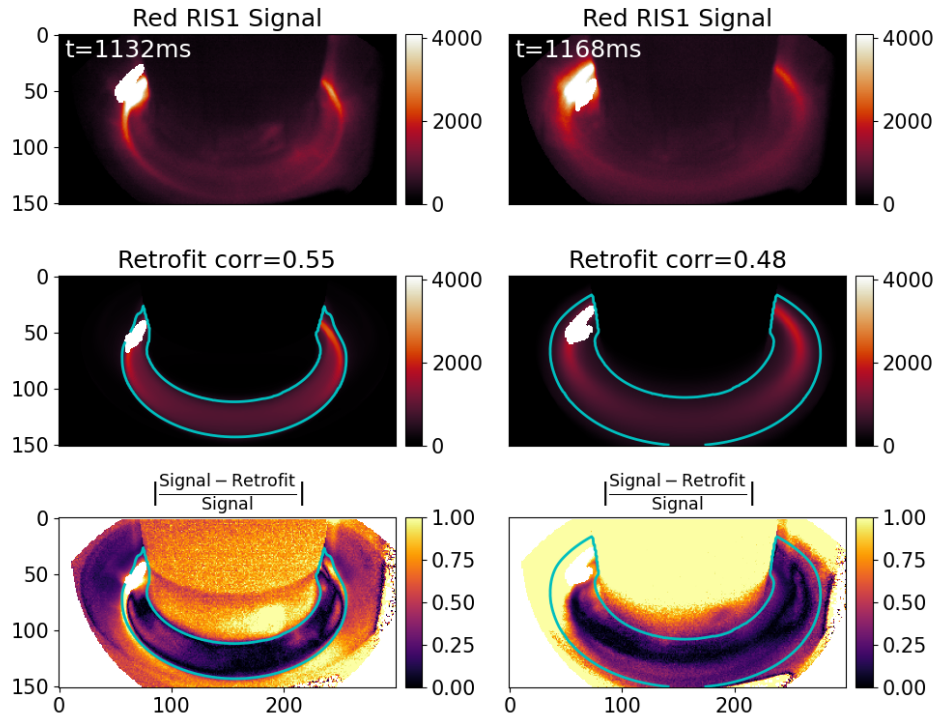


Figure 5.5: Comparison of reconstructed RIS1 view from discharge #15977. The top row shows the red RIS1 signals, the middle row shows the red MFR RIS2 retrofits multiplied by correlation coefficients (corr), and the bottom row shows the normalised difference between the signal and retrofit. The areas of interest are highlighted by cyan contour.

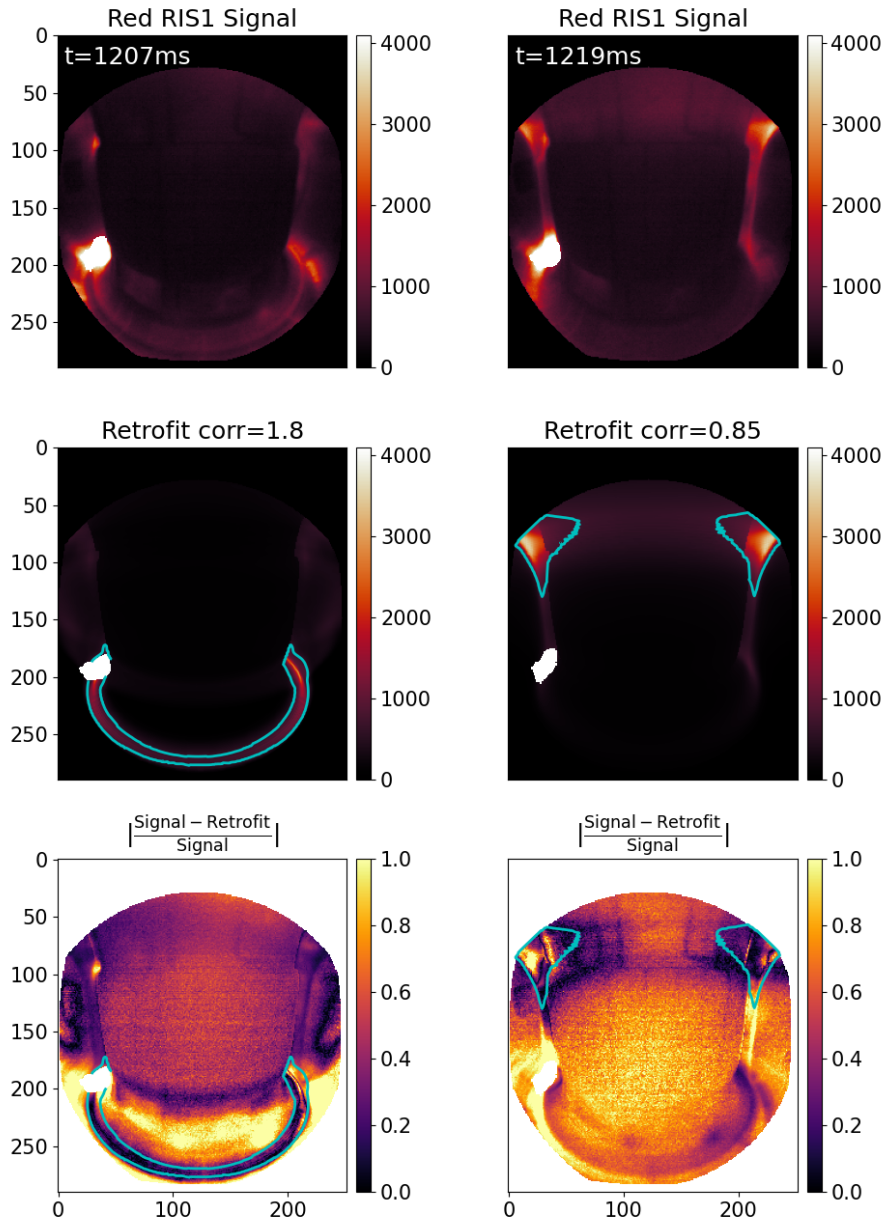
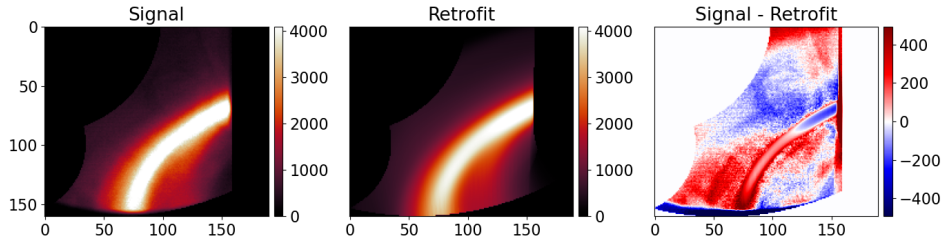


Figure 5.6: Comparison of reconstructed RIS1 view from discharge #20919. The top row shows the red RIS1 signals, the middle row shows the red MFR RIS2 retrofits multiplied by correlation coefficients (corr), and the bottom row shows the normalised difference between the signal and retrofit. The areas of interest are highlighted by cyan contour.

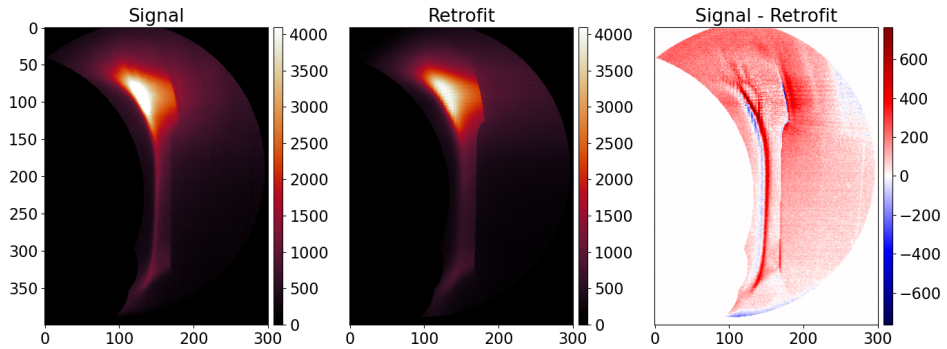
5.4 Discussion on the accuracy of the reconstructions

As was shown in previous sections, the emissivity reconstructions for both discharges seemed successful and quite accurate. However, no comparison between the retrofit and the input image were shown yet. For this, the red pixels and their MFR reconstructions were used, as the red colour was least saturated and the MFR reconstruction was the smoothest. Additionally, because the MFR and BoB reconstructed the same nitrogen detachment front, the conclusions for comparisons could be to some extent applied for both methods.

The two examples of red signals, retrofits of their MFR reconstructions and their difference are shown in Fig. 5.7 for each shot.



(a) : Discharge #15977, $t = 1150.3\text{ms}$.



(b) : Discharge #20919, $t = 1219.625\text{ms}$.

Figure 5.7: The figure shows the red signals, their MFR reconstructions retrofit, and their differences for discharges #15977 and #20919 from left to right. The maximal/minimal values of difference were lowered to better visualise areas of interest (nitrogen detachment front).

For the discharge #15977, the discrepancy between the signal and the retrofit can be seen mainly near the central column and bottom of the divertor. The discrepancy on the bottom is caused by a small part of port that was not fully masked in the image, leaving zero values, explaining the negative values in the difference. The area around the central column has a bigger discrepancy, probably because of a slightly inaccurate camera calibration.



Summary and conclusion

The aim of this thesis was to diagnose detachment experiments at the COMPASS tokamak using visible cameras and tomographic inversion. Specifically, two types of experiments, with forward and reversed fields, were studied and compared to account for the possible effect of drifts on the movement of the radiative cloud that appears in detachment experiments.

The thesis begins with a general description of the tokamak and the divertor detachment, followed by a brief explanation of the tomographic inversion techniques. The second chapter gives an overview of the detachment experiments conducted on the COMPASS tokamak, providing background information about the data that were analysed. Procedures used for camera tomography of tokamak plasmas are described in chapter 3, where the Minimum Fisher Regularisation (MFR) and the BiOrthogonal Decomposition (BoB) inversion methods are explained in more details. Data processing with encountered issues and their solutions are discussed in the fourth chapter. The results from the performed tomography are then presented and discussed in the last chapter.

In the scope of this thesis, a successful tomographic inversion of visible camera data was performed for the two different discharges, assuming toroidal symmetry of the observed events. This required following steps:

1. Performing precise camera calibration in Calcam software to obtain modelled camera views.
2. Selecting relevant pixel areas to be used for the inversion and masking others to remove the effect of non toroidally symmetry features (reflections, noise, etc.).
3. Using two different tomographic inversion algorithms from the Python package Tomotok, namely MFR (regularised) and BoB (unregularised).
4. Analysing the assumption of toroidal symmetry by comparing the tomography results obtained with a narrow view camera and the data from a larger camera view.

The results could be further improved by including a model of reflections on PFCs, having a CAD model representing the vessel more accurately,



Bibliography

- [1] F. Cappelletti, “The promise of magnetic fusion for a sustainable future - policy paper,” July 2022.
- [2] Y. Li, “Thermo-mechanical behavior of tungsten under fusion-relevant hydrogen plasma loads,” *PhD thesis*, June 2021.
- [3] FusionWiki, “Divertor, Separatrix, Scrape-Off Layer, Detachment,” <http://fusionwiki.ciemat.es>. [Online; accessed 7-July-2023].
- [4] P. Rindt *et al.*, “Conceptual design of a liquid-metal divertor for the European DEMO,” *Fusion Engineering and Design*, vol. 173, p. 112812, 2021.
- [5] G. Ambrosino *et al.*, “Plasma Strike-Point Sweeping on JET Tokamak with the eXtreme Shape Controller,” *IEEE Transactions on Plasma Science*, vol. 36, no. 3, pp. 834–840, 2008.
- [6] R. Perillo *et al.*, “The influence of N₂ and H₂ seeding on detachment in a divertor-relevant plasma by means of modelling and experiments in Magnum-PSI,” in *44th EPS Conference on Plasma Physics (EPS 2017)*, June 2017.
- [7] J. Gunn *et al.*, “Surface heat loads on the ITER divertor vertical targets,” *Nuclear Fusion*, vol. 57, p. 046025, March 2017.
- [8] Art, n.1, “Oxford English Dictionary Online”. *Oxford University Press*, 2023.
- [9] Wikipedia, “Tomography - Wikipedia, the free encyclopedia.” <https://en.wikipedia.org/wiki/Tomography>, 2023. [Online; accessed 13-July-2023].
- [10] B. Kelley *et al.*, “The fast discrete Radon transform. I. Theory,” *IEEE Transactions on Image Processing*, vol. 2, no. 3, pp. 382–400, 1993.
- [11] L. Ingesson *et al.*, “Chapter 7: Tomography Diagnostics: Bolometry and Soft-X-Ray Detection,” *Fusion Science and Technology*, vol. 53, pp. 528–576, February 2008.

Appendix A

Additional figures

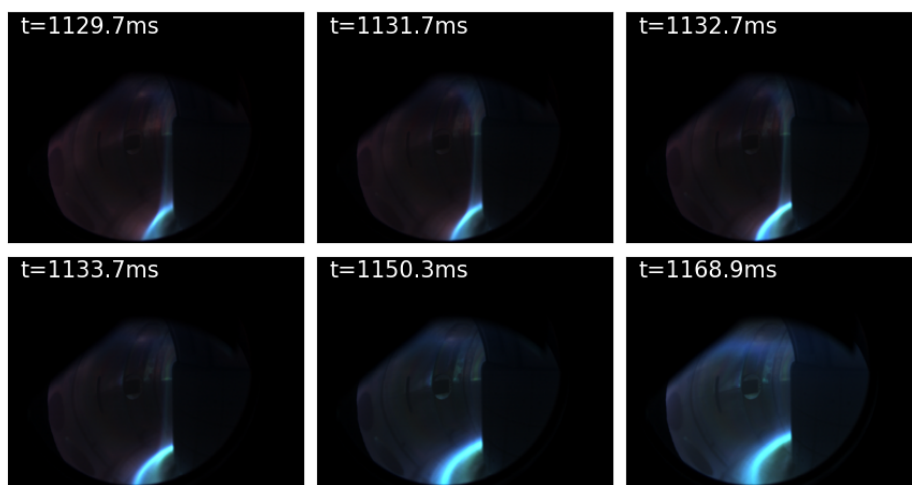


Figure A.1: Used images for the tomographic inversion from discharge #15977.

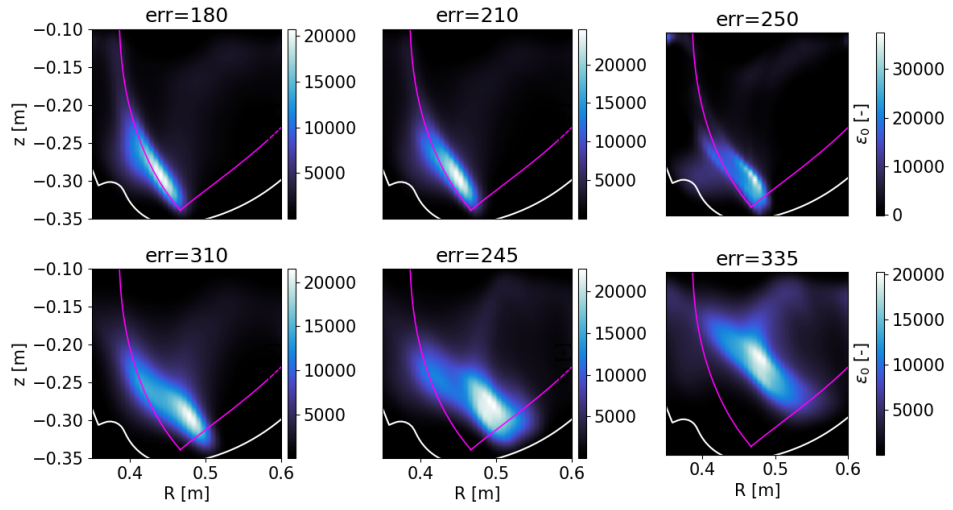


Figure A.2: MFR inversions with estimated error (*err*) for only blue coloured pixels from discharge #15977.

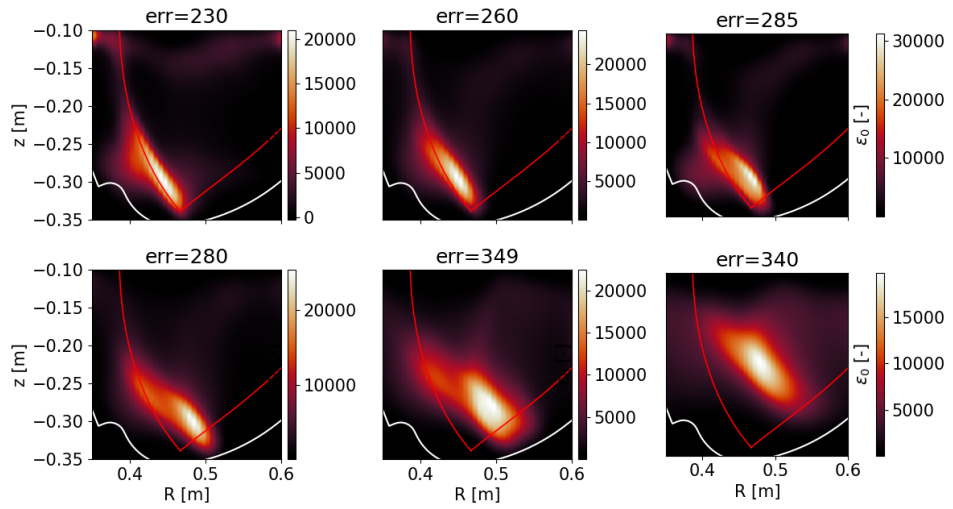


Figure A.3: MFR inversions with estimated error (*err*) for only red coloured pixels from discharge #15977.

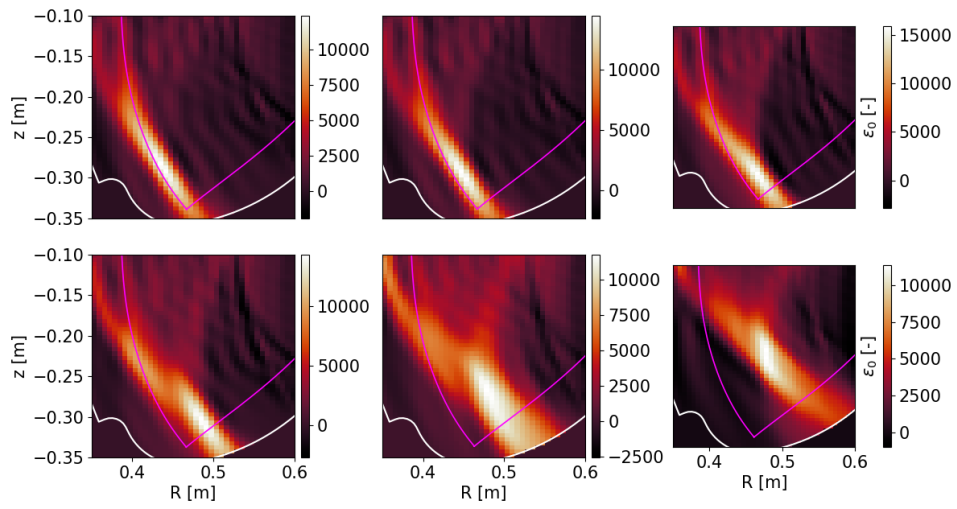


Figure A.4: BoB inversions for only red coloured pixels from discharge #15977.

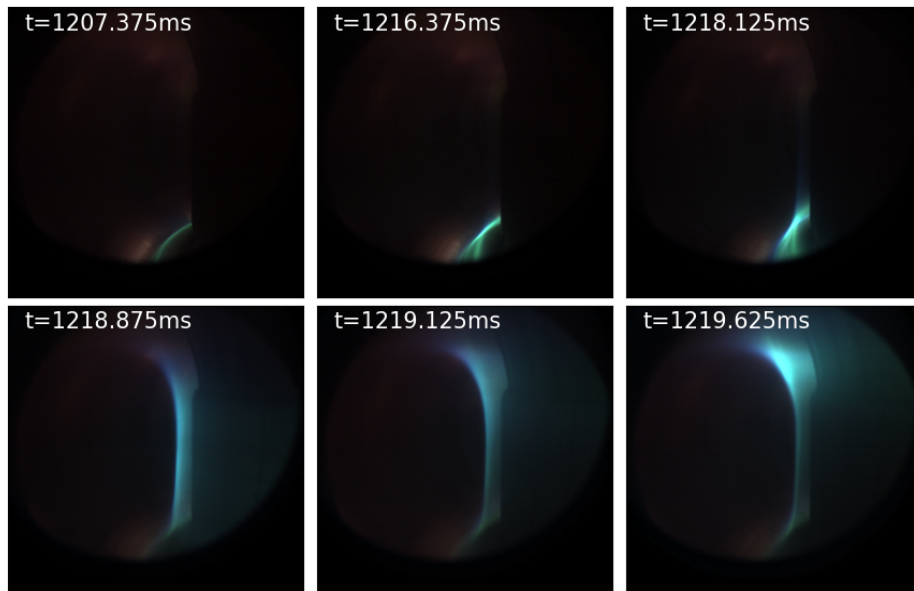


Figure A.5: Used images for the tomographic inversion from discharge #20919.

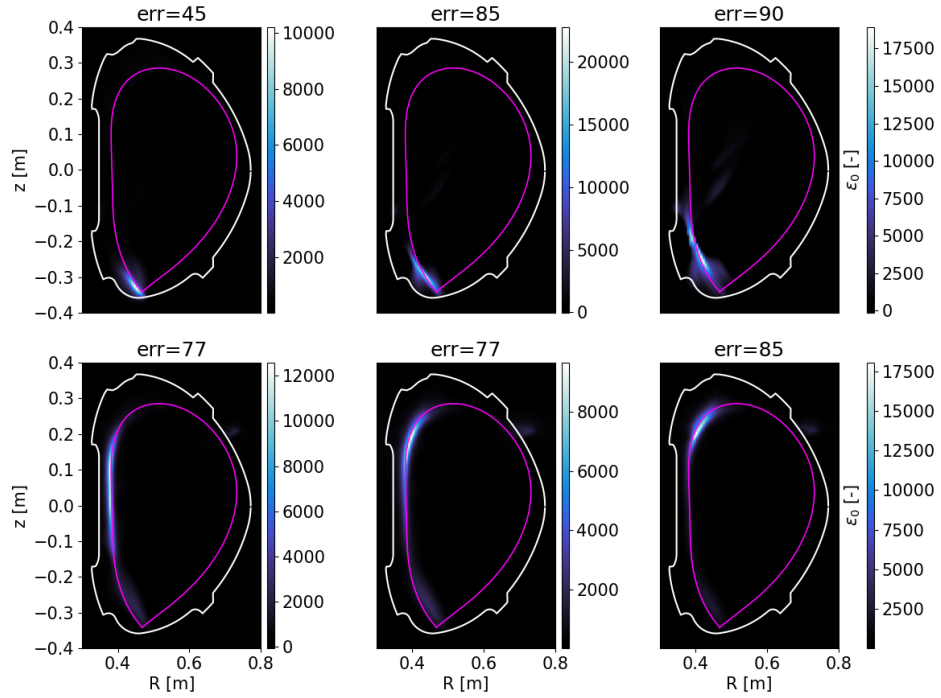


Figure A.6: MFR inversions with estimated error (*err*) for only blue coloured pixels from discharge #20919.

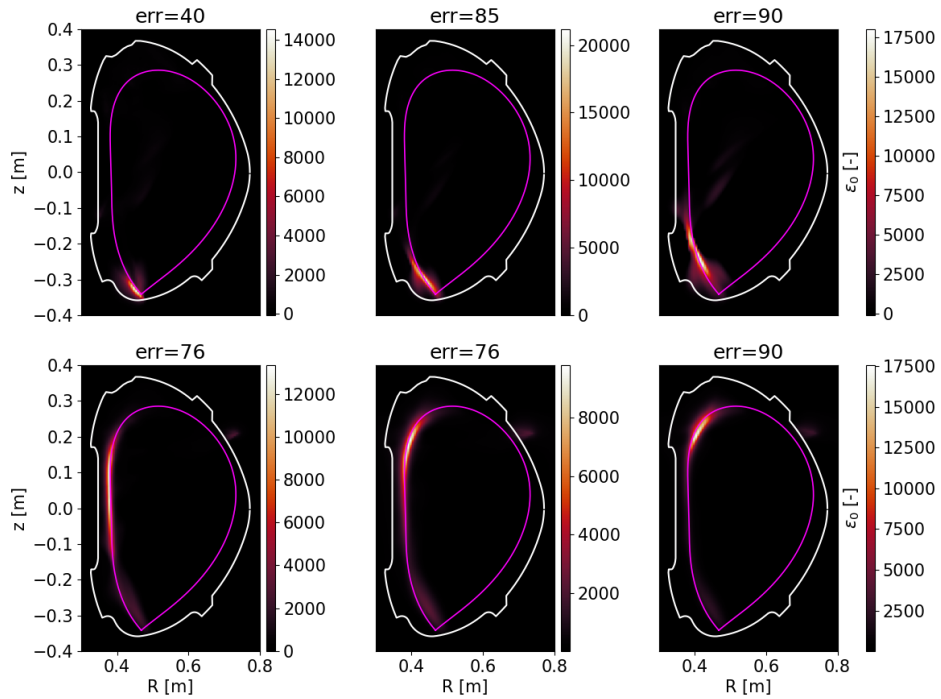


Figure A.7: MFR inversions with estimated error (*err*) for only red coloured pixels from discharge #20919.

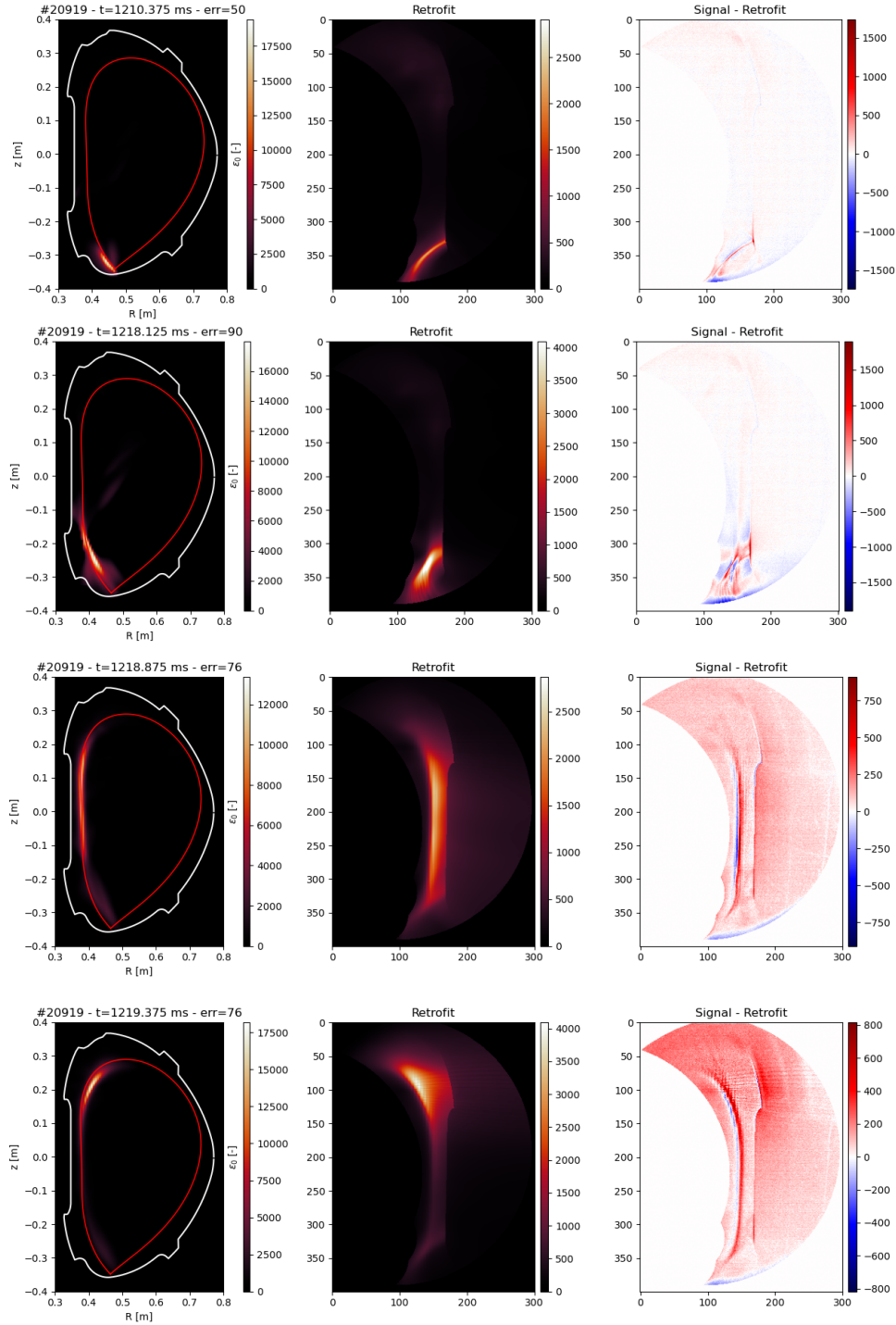


Figure A.8: MFR inversions with estimated error (err) for only red coloured pixels from discharge #20919, with their retrofits and comparison with red signals.